

Capacity Analysis of Adaptive IRS-Aided Transmission with Direct Link in Nakagami- m Fading Channels

Ashraf Al-Rimawi, *Member, IEEE*, Arafat Al-Dweik, *Senior Member, IEEE*, and Ali Siddig, *Member, IEEE*

Abstract—This paper introduces a new analytical framework to evaluate the capacity of intelligent reconfigurable surface (IRS)-aided wireless networks in the presence of a direct link (DL). The analysis obtained is used to characterize the signal-to-noise ratio (SNR) at the user equipment (UE) while using adaptive power and rate transmission. In particular, we consider channel inversion with fixed rate, optimum power and rate adaptation, and truncated channel inversion with a fixed rate. The obtained expressions are derived in a unified closed-form. All single-hop channel gains are modeled as independent and identically distributed Nakagami- m fading channels. Consequently, the channels' gains at the receiver become independent and nonidentically distributed. The moment generating function (MGF) is used to derive an accurate approximation of the probability density and cumulative distribution functions of the instantaneous SNR, which are used to evaluate the channel capacity at low and high SNRs to quantify the achievable multiplexing gain. The analytical and simulation results obtained indicated that a strong DL may significantly enhance the channel capacity gain obtained using the IRS. In particular scenarios, the capacity improved by approximately 30% for a large number of IRS elements when the DL Nakagami fading parameter m increases from 2 to 6.

Index Terms—intelligent reconfigurable surface (IRS), Nakagami- m , capacity, moment generating function (MGF), outage probability (Pout), sixth generation (6G), millimeter wave (mmW)

I. INTRODUCTION

THE demand for higher mobile transmission capacity has increased exponentially in the last few years. According to the Cisco Mobility Report [1], about 70% of the global population will have mobile connectivity by 2023, where the total number of global mobile users will increase from 5.1 billion in 2018 to 5.7 billion in 2023. Furthermore, the total number of mobile devices will increase by about 48% over the same period, reaching about 13 billion. The main drivers of the continuously increasing demand for capacity are the significant increase in mobile-connected devices and the emergence of services that require high data rates, such as high-quality video streaming over mobile networks. According to the Cisco report, the fastest growing category of mobile devices is

machine-to-machine (M2M) followed by smartphones. Consequently, a key solution for emerging wireless communications standards is the migration to higher frequencies, such as the millimeter wave (mmW) frequency bands. Such bands provide a bandwidth of several GHz and allow transmission of data rates at multi-Gbit/s.

Despite the many advantages of mmW communications, there are some fundamental challenges associated with its use. One of these challenges is that mmW communication devices use narrow directional beams to maintain the connection, which implies that the transmitter and receiver must continually adjust their beam direction to maintain alignment as the user moves. Additionally, even small objects can block the mmW communication link from the base stations (BS) to the user equipment (UE). To mitigate severe signal attenuation, various techniques have been proposed, among which intelligent reconfigurable surface (IRS) is considered a profound candidate [2], [3]. IRS, however, have recently received enormous attention as a promising technology for future wireless communications to improve the coverage and capacity of the wireless network through intelligent reconfiguration of the wireless propagation environment [4]–[10]. In particular, by properly programming its assumed phase shifts, IRS can intelligently control the wireless channel and thus give it a performance boost [11]–[13]. Furthermore, IRSs consume much less energy and have lower hardware costs since they do not require radio-frequency (RF) chains, making them more cost-effective and environmentally friendly than multi-antenna and relaying systems [5], [14], [15].

Various channel models have been proposed that encompass the statistical properties of a typical IRS-assisted mmW communications links [16]. Specifically, the Nakagami- m channel model is found to be more suitable for IRS-assisted mmW communications because both BS to IRS and IRS to mobile user (MU) mmW links have relatively a strong line-of-sight (LOS) element further to the non-line-of-sight (NLOS) scattering components [17]–[20]. Moreover, it is a more versatile statistical model [21] that can represent various fading scenarios, including those represented by the Rayleigh, Rician, and one-sided Gaussian fading models. Furthermore, the Nakagami- m distribution can be controlled to suit experimental measurements for various practical channels [22].

Ashraf Al-Rimawi is with the Department of Electrical and Computer Engineering, Birzeit University, Palestine. (e-mail: aalrimawi@birzeit.edu).

Arafat Al-Dweik is with the 6G Research Center, Department of Computer and Communications Engineering, Khalifa University, Abu Dhabi, UAE. (E-mail: arafat.dweik@ku.ac.ae, dweik@fulbrightmail.org).

Ali Siddig is with the Department of Computer and Communications Engineering, Khalifa University, Abu Dhabi, UAE. (ali.siddig@ku.ac.ae).

A. Related Work

In the literature, IRS-aided systems have been extensively studied in [5], [20], [23]–[33]. [5] provides an overview of the state-of-the-art solutions, most significant open research issues, and the main important differences between IRS and other technologies. Additionally, most of the research on IRS-assisted wireless communication systems focuses on the design [23], [24], optimization [20], [25]–[28] and possible applications [29]–[31], while the theoretical study of IRS-assisted wireless communication networks is still in its early stages where few studies have been conducted to evaluate the performance of such systems due to the difficulty of statistically characterizing the signal-to-noise ratio (SNR) at the UE. Therefore, several approximations, asymptotic analyses or bounds have been developed to analyze the IRS-assisted wireless communications systems [34]–[36].

Based on the received signal sources, the system model can be generally classified into two main categories: IRS without a direct signal from the BS to the UE [5], [12], [35]–[50], which is widely adopted in the literature, and with a direct link (DL) [51]–[60]. Tables I and II show the classification of some state-of-the-art articles based on their consideration of direct and indirect links, system/channel model, and metric used to describe the system performance. The abbreviations used in the tables are error probability (EP), outage probability (OP), coverage probability (CP), perfect phase knowledge (P-phase), single-input single-output (SISO), multiple-input multiple-output (MIMO), and ergodic capacity (EC).

1) *IRS without DL*: The authors in [5], [12], [35], [36], [42]–[47] model the overall IRS channel gain Gamma [12], as Nakagami- m [42], and Rayleigh [5], [44], and then provide exact and approximate closed-form expressions based on various performance metrics. Additionally, the Central Limit Theorem (CLT), which is used to represent the channel [43], is inaccurate when a few reflecting elements are allocated. The Fox-H function is used to create a generalized analytical framework in [46], which has been shown to be accurate even for a small number of reflecting elements, especially when the applied phase shift is continuous.

2) *IRS with DL*: In [51]–[53], [55]–[58], the authors consider the performance analysis of IRS systems with a DL, where the SNR at the UE is approximated using various methods, including the CLT. The channel model in [52], [53], [55]–[58] is regarded as Nakagami- m , Rician, and Rayleigh, as given in Table II. Moreover, the Rician and K -fading models are both taken into account in [51]. Generally speaking, most of the analytical work derived in the literature for the IRS with DL considers approximations based on a large number of reflectors to validate invoking the CLT. Therefore, the obtained accuracy could be low for small and moderate numbers of reflectors [52]–[56], [58]–[60]. In [51], the author used the $N \rightarrow \infty$ approximation. However, the numerical results provided show that the approximation might have low accuracy in certain cases. The work in [57] derived an upper bound for the ergodic capacity, which can deviate noticeably from the exact capacity. In [58] only the outage is derived based on CLT, and the results are presented for the case of 32 reflectors,

yet some discrepancies can be observed between the analytical and simulation results in some scenarios.

On the other hand, the cases of multiple IRS panels have been considered as reported in [61], [62]. The authors in [61] considered two modes of operation, energy harvesting and information processing, and evaluated the impact of the IRS location on the system performance. In the information processing mode, the system model does not consider the DL between nodes S and D . Moreover, the composite channel after phase compensation and superposition of the reflected signals is modeled as a Nakagami- m channel. In addition, capacity analysis is not considered; instead, outage probability and throughput are derived with fixed transmission power. Tran *et al.* [62] considered multiple IRS panels with a DL where all channels' gains are modeled as Nakagami- m fading channels. The authors derived accurate expressions for the outage probability, throughput, achievable data rate, and symbol error probability with and without hardware impairments. The probability density function (PDF) and cumulative distribution function (CDF) of the SNR are derived in closed-form using the Gamma approximation. The PDF and CDF for the single IRS case are derived for the generalized κ - μ channel [63]. By noting that the Nakagami- m can be considered as a special case of κ - μ fading, then the PDF of the Nakagami- m case can be derived as a special case of [63, Eq. (28)]. Nevertheless, the obtained PDF is expressed in the form the product of exponential and confluent hyper-geometric function, which makes the analysis intractable. Moreover, capacity and adaptive transmission are not considered in [63].

B. Motivation and Contribution

As can be noted from the extensive literature search, and to the best of the authors' knowledge, the capacity and outage analysis of IRS-assisted communications from an information-theoretic aspect is partially addressed. Evaluating the outage and capacity of IRS systems is critical to guide future theoretical and experimental research in this field because it outlines the boundaries and limits that the system can approach under various operating conditions. The amount of fading is also a useful metric for evaluating the effectiveness of the system in mitigating the severity of channel fading [69, pp. 12]. It is also crucial to derive the necessary tools such as the PDF, CDF, and moment generating function (MGF) to enable analytical derivation of the metrics mentioned above. As depicted in Sec. I, the vast majority of the studies ignore the DL between the BS and UE [12], [26], [37]–[39], [43]–[47], [49], [50], [64]. For the articles that consider the DL, they do not consider the impact of the various transmission strategies that can be adopted [27], [51]–[57], [65]. To cover such a research gap, the core contributions of this article are:

- 1) Presents a novel framework to theoretically compute the channel capacity of the IRS-aided transmission while considering the impact of the BS-UE DL.
- 2) Derives the MGF and uses it to derive closed-form expressions for the amount of channel fading, the CDF and PDF are derived and used to characterize the behavior of SNR at the UE front-end.

Table I: References without a DL.

Ref	EC	OP	EP	Ant.	Approach	Channel	P-Phase	Mod.
[5]	–	✓	–	SIMO	CLT	Rician	✗	–
[12]	✓	✓	✓	SISO	Gamma distribution	Rayleigh	✓	QAM
[35]	–	✓	✓	SISO	Gamma distribution	Nakagami- m	✗	BPSK, QPSK
[36]	–	–	✓	SISO	Nakagami- m	Arbitrary	✗	BPSK
[37]	✓	✓	✓	SISO	CLT	Rayleigh	✓	DBPSK
[38]	✓	✓	✓	SISO	Leveraging Theorem	Rician	✓	QAM
[39]	✓	–	–	MIMO	CLT	Rician	✓	–
[40]	–	–	✓	SISO	CLT	Rayleigh	✓	QAM
[41]	–	✓	–	SIMO	CLT	Rician	✗	–
[42]	–	✓	✓	SISO	K -distribution	Rician	✓	QAM
[43]	✓	✓	✓	SISO	CLT	Rayleigh	✓	QAM
[44]	✓	✓	✓	MIMO	K_G distribution	Rayleigh	✓	DPSK
[45]	✓	✓	–	SISO	Gamma distribution	Fox's H	✓	–
[46]	–	✓	–	SISO	Asymptotic	Fox's H	✗	–
[47]	✓	–	–	MIMO	CLT	Deterministic	✗	–
[48]	–	✓	✓	SISO	CLT	Rayleigh	✗	DBPSK
[49]	✓	✓	✓	SISO	Gamma-distribution	Rayleigh	✗	BPSK
[50]	✓	–	–	MISO	Upper bound	Rayleigh, Rician	✓	–
[64]	✓	✓	✓	MIMO	CLT	Nakagami- m	✗	DBPSK
[65]	✓	✓	✓	MIMO	Laguerre series	κ - μ	✗	QAM

Table II: References with DL, SISO is considered for all cases.

Ref	EC	OP	EP	Methodology	Channel	P-Phase	Modulation	Adaptive Power
[51]	✓	✓	✓	Approx. ($N \rightarrow \infty$)	K -distribution, Rician	✓	BPSK	✗
[52]		CP		CLT	Nakagami- m	✓	–	✗
[53]	✓	–	–	CLT	Rayleigh	✓	–	✗
[54]	✓	–	–	CLT	Rayleigh	✓	–	✗
[55]	✓	–	–	CLT	Rayleigh	✗	–	✗
[56]	✓	✓	–	CLT	Rayleigh	✗	–	✗
[57]	✓	✓	–	Leveraging Theorem	Rician	✓	–	✗
[58]	–	✓	–	CLT	Nakagami- m	✓	–	✗
[59]	–	✓	–	CLT	Rayleigh	✓	–	✗
[60]	–	–	✓	CLT	Nakagami- m	✗	QAM	✗
This work	✓	✓	–	Laplace	Nakagami- m	✓	–	✓

Table III: List of functions, $\mathbf{a}_p = a_1, \dots, a_p$; $\mathbf{b}_q = b_1, \dots, b_q$.

Symbol	Function	Symbol	Function
$E[\cdot]$	Statistical expectation	$C_{p,q}^{m,n}(\cdot)$	Meijer's G function [66, sec. 9.3]
$Var(\cdot)$	Statistical variance	$B(\cdot, \cdot)$	Beta [66, eq. (8.38)]
$Pr[\cdot]$	Probability operation	${}_pF_q(a_p; b_q; x)$	Generalized hypergeometric function (HF) [66, eq. (9.14)]
$L[\cdot]$	Laplace	${}_1F_1(\cdot; \cdot; \cdot)$	Confluent HF [66, eq. (8.310)]
$L^{-1}[\cdot]$	Laplace Inverse	${}_1F_1(\cdot)$	Regularized HF
$M_v(\cdot)$	MGF	Φ_2	Bivariate confluent hypergeometric [67]
$f_X(\cdot)$	PDF	$K_v(\cdot)$	Modified Bessel of order v [68, eq. (9.6.2)]
$F_X(\cdot)$	CDF	$\gamma(\cdot, \cdot)$	Lower incomplete gamma [66, eq. (8.350)]
$\Gamma(\cdot)$	gamma [66, eq. (8.310)]		

- 3) Closed-form expressions are derived for the outage probability and channel capacity under various adaptive transmission models, which are the Optimum Rate Adaptation (ORA), Optimum Power and Rate Adaptation (OPRA), Channel Inversion with Fixed Rate (CIFR), and Truncated Inversion with Fixed Rate (TIFR).
- 4) The derived expressions are used to evaluate the system performance for various values of the Nakagami- m fading parameter, and the number of reflecting IRS elements.
- 5) To gain more insight into system performance, an accurate closed-form expression is derived for the asymptotic channel capacity for the ORA as well as the multiplexing gain.
- 6) The analytical formulas obtained are validated using

extensive Monte Carlo simulation results.

The obtained analytical and simulation results show that the application of optimum power should be performed while considering the number of reflectots and the strength of the direct and reflected signals. In particular scanrios, the use of power optimization becomes inefficient due to the small gain that it offers in proportion to the additional overhead and complexity.

C. Paper Organization and Notations

The remainder of this work is organized as follows. Sec. II presents the IRS-based network model and describes the models of the channels considered. The section also presents the PDF of the received signal power, the MGF and CDF of the

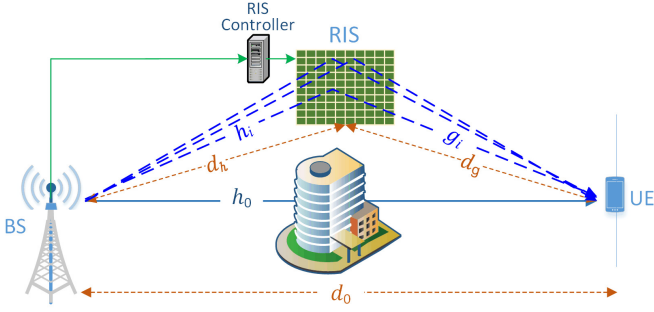


Figure 1: Model of the IRS system with direct and reflected links. For the DL, h_0 and d_0 are the gain and distance of the channel, respectively. With regard to the i th reflecting element, h_i and d_i of the BS-IRS link channel gain and distance, respectively, are $i > 0$. The IRS-UE link distance and channel gain are d_g and g_i , respectively.

overall channel gain, and the PDF of the SNR at the UE. Sec. II-G presents the amount of fading derivation and discussion while Sec. III presents the capacity analysis with adaptive transmission. Sec. IV includes the numerical results for various network and fading scenarios and provides insight into the pivotal and nonintuitive results. Finally, Sec. V outline the main conclusions of the paper, Sec. VI presents the appendices. Table III summarizes the main functions used throughout the paper.

II. SYSTEM AND CHANNEL MODELS

A. System Model

This work considers a wireless communications network where an IRS panel is used to assist the communications between a BS and a UE. The network model is depicted in Fig. 1 where the IRS panel is equipped with N reflecting elements used to reflect the BS signals toward the UE. Although the IRS can be initially placed such that the UE receives only the signals reflected from the IRS panel, some of the UEs may change their location where they may receive the BS signal through two different links, a DL from the BS and a reflected link through the IRS panel. Moreover, given that adjacent IRS elements are distant by at least half the carrier signal wavelength, the channel gains for all IRS elements can be assumed to be not independent and identically distributed (n.i.i.d.). The fading channel gain of the BS-IRS link is denoted as h_i , and the IRS-UE link gain is denoted as g_i , where $i \in \{1, 2, \dots, N\}$. The distances BS-to-IRS and IRS-to-UE are considered sufficiently large and the number of reflecting elements N is relatively small, and hence all channels' gains follow the far-field model [70].

The channel state information (CSI) for all links can be communicated to the BS through a dedicated feedback channel. At the UE side, the CSI can be estimated using various blind or data-aided channel estimation methods [5], [11], [26], [71]–[73]. Although the CSI can not be estimated perfectly, it has been shown in [29] that IRS systems are generally more tolerant to channel estimation errors compared to non-IRS based systems. Therefore, we consider the channel gains to be perfectly estimated and compensated at the IRS panel. Moreover, this assumption is widely adopted to make the

analysis tractable [29]. Consequently, using a single-antenna setup at all devices, the signal at a given UE front-end can be written as

$$Y = Y_D + Y_R + n \quad (1)$$

where Y_D represents the signal component received through the DL, Y_R is the signal reflected by the IRS, and $n \sim \mathcal{CN}(0, N_0)$ is the additive white Gaussian noise (AWGN). The DL signal component can be expressed as [52]

$$Y_D = \sqrt{P} |h_0| e^{-j\theta_0} s \quad (2)$$

where P is the transmission power, s is the data symbol, $|h_0|$ and θ_0 are the amplitude and phase of the BS-UE channel.

Similarity, Y_R denotes the received signal component at the UE front-end through the IRS panel, which can be expressed as

$$Y_R = \sqrt{P} s \sum_{i=1}^N |h_i| |g_i| e^{-j\theta_i} v_i e^{j\Psi_i} e^{-j\phi_i} \quad (3)$$

where $|h_i|$ and θ_i are the amplitude and phase of the BS-IRS link h_i , respectively, while, $|g_i|$ and ϕ_i are the amplitude and phase of the IRS-UE link g_i , respectively. Therefore, the channel model considers small-scale fading, which is widely adopted in the literature [12], [38], [74]. The large-scale fading due to path-loss can also be included as described [75], [76].

The i th IRS element gain and phase shift are given by v_i and Ψ_i , however, v_i is typically considered fixed and equals one [12], [29], [77]–[79]. Therefore,

$$Y_R + Y_D = \left(\sum_{i=1}^N |h_i| |g_i| e^{-j\Phi_i} + |h_0| \right) s \sqrt{P} e^{-j\theta_0} \quad (4)$$

where $\Phi_i = \phi_i + \theta_i - \Psi_i - \theta_0$. For analysis tractability, the phases of the IRS elements are selected such that the phases of the direct and reflected signals add coherently to maximize the SNR, i.e., $\Phi_i = 0$ [5], [25], [32], [77], thus

$$\begin{aligned} Y_R + Y_D &= \sqrt{P} e^{-j\theta_0} \left(\sum_{i=1}^N |h_i| |g_i| + |h_0| \right) s \\ &= (H_R + H_D) e^{-j\theta_0} s. \end{aligned} \quad (5)$$

Therefore, the composite channel gain can be formulated as

$$V = H_D + H_R \quad (6)$$

where $H_D = \sqrt{P} |h_0|$, and $H_R = \sqrt{P} \sum_{i=1}^N |h_i| |g_i|$.

Therefore, even though the DL phase cannot be controlled, it is still possible to coherently combine the direct and IRS-reflected signals at the UE. It should be noted that the impact of phase estimation and compensation errors on capacity is investigated in [79] where it is shown that IRS can tolerate a certain level of errors without significant capacity loss.

B. Channel Model

the Nakagami- m PDF is widely used to model fading channels with various severeness while offering a simple physical interpretation and flexible analytical representation. Moreover, there are widely used fading models that are special cases of the Nakagami- m distribution. For example, the one-sided

Gaussian distribution is equivalent to the Nakagami where $m = 0.5$ and the Rayleigh where $m = 1$. Moreover, the Rician can be approximated by the Nakagami- m by using the appropriate parameter transformation [22], [80]. In the context of IRS the Nakagami-Rician approximation becomes more accurate for a large number of reflecting elements. In addition, it can be used with applications such as satellite and vehicle-to-vehicle communications. By restricting the fading parameter m to integer values, negligible differences are obtained for several cases of interest while simplifying mathematical analysis and enabling the derivation of closed-form formulas [81]. Consequently, we consider all channel gains in this work to be Nakagami- m distributed with an integer m . The Nakagami- m PDF can be expressed as [21]

$$f_X(x) = \frac{2}{\Gamma(m)} \left(\frac{m}{\Omega}\right)^m x^{2m-1} e^{-\frac{x^2}{\Omega}} \quad (7)$$

where the fading parameter m is defined as

$$m = \frac{\mathbb{E}^2[x^2]}{\text{Var}[x^2]}$$

and $\mathbb{E}[\cdot]$ denotes the statistical expectation while $\Omega = \mathbb{E}[x^2]$ is the second moment. The Nakagami- m with parameters m and Ω will be denoted as $\mathcal{NK}(m, \Omega)$.

C. PDF of the Received Signal Power

As can be seen from (5) and (6), the instantaneous power of the received signal is V^2 . To derive its PDF, define $|h_i||g_i| \triangleq Z_i$. To simplify the notation, the reflector index i will be neglected unless it is necessary to explicitly include it. Therefore, the PDF of Z is given by [82],

$$f_Z(z) = \int_0^\infty \frac{1}{x} f_h(x) f_g\left(\frac{z}{x}\right) dx. \quad (8)$$

By substituting the PDFs $|h| \sim \mathcal{NK}(m_1, \Omega_1)$, and $|g| \sim \mathcal{NK}(m_2, \Omega_2)$ expressed in (7), into (8), and using the identity [66, eq. (3.471.9)] gives

$$\int_0^\infty x^{v-1} e^{\frac{\beta}{x} - \gamma x} dx = 2 \left(\frac{\beta}{\gamma}\right)^{\frac{v}{2}} K_v\left(2\sqrt{\beta\gamma}\right) \quad (9)$$

we obtain,

$$f_Z(z) = \frac{4}{\Gamma(m_1)\Gamma(m_2)} \left(\frac{m_1 m_2}{\Omega_1 \Omega_2}\right)^{\frac{m_1+m_2}{2}} \times z^{m_1+m_2-1} K_{m_1-m_2}\left(2\sqrt{\frac{m_1 m_2}{\Omega_i \Omega_j}} z\right). \quad (10)$$

where $K_v(\cdot)$ denotes Modified Bessel of order v [68, eq. (9.6.2)]. Moreover, the first and second moments of Z are respectively given by,

$$\mathbb{E}[Z] = \sqrt{\frac{\Omega_1 \Omega_2}{m_1 m_2}} \frac{\Gamma(m_1 + \frac{1}{2})}{\Gamma(m_1)} \frac{\Gamma(m_2 + \frac{1}{2})}{\Gamma(m_2)} \triangleq \mu_Z \quad (11)$$

and

$$\mathbb{E}[Z^2] = \frac{\Omega_1 \Omega_2}{m_1 m_2} \frac{\Gamma(m_1 + 1)}{\Gamma(m_1)} \frac{\Gamma(m_2 + 1)}{\Gamma(m_2)}. \quad (12)$$

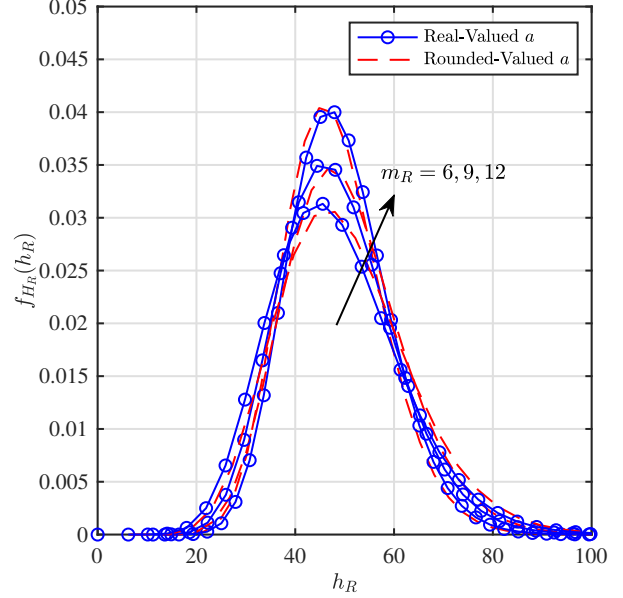


Figure 2: The PDF $f_{H_R}(h_R)$ for $m_R = 6, 9$ and 12 . Solid lines correspond to real-valued $a \in 11.5, 17.5, 13.5$, whereas dashed lines correspond to the rounded values of $a \in 12, 18, 24$; $N = 50$.

From (11) and (12), the variance of Z can be written as

$$\text{Var}[Z] \triangleq \sigma_Z^2 = \mathbb{E}[Z^2] - (\mathbb{E}[Z])^2. \quad (13)$$

In the case that $m_1 = m_2 = m_R$ and $\Omega_1 = \Omega_2 = \Omega_R$, then

$$f_Z(z) = \frac{4}{[\Gamma(m_R)]^2} \left(\frac{m_R}{\Omega_R}\right)^{2m_R} z^{2m_R-1} K_0\left(\frac{2m_R}{\Omega_R} z\right) \quad (14)$$

$$\mu_Z = \frac{\Omega_R}{m_R} \left[\frac{\Gamma(m_R + \frac{1}{2})}{\Gamma(m_R)}\right]^2, \quad (15)$$

and

$$\sigma_Z^2 = \left[\frac{\Omega_R}{m_R \Gamma(m_R)}\right]^2 \left[\Gamma^2(m_R + 1) - \frac{\Gamma^4(m_R + \frac{1}{2})}{\Gamma^2(m_R)}\right]. \quad (16)$$

However, using the exact PDF $H_R = \sum_{i=1}^N Z_i$ and the moments of H_R leads to computationally complex and intractable analysis.

Therefore, we use the approximation in [44] to simplify $f_{H_R}(h_R)$ by using the gamma distribution [63],

$$f_{H_R}(h_R) = \frac{(h_R)^{a-1}}{b^a \Gamma(a)} \exp\left(-\frac{h_R}{b}\right) \quad (17)$$

where $a = \frac{\mu_{H_R}^2}{\sigma_{H_R}^2}$, $b = \frac{\sigma_{H_R}^2}{\mu_{H_R}}$, $\mu_{H_R} = \sum_{i=1}^N \mu_{Z_i}$ and $\sigma_{H_R}^2 = \sum_{i=1}^N \sigma_{Z_i}^2$. In case of independent and identically distributed (i.i.d.) channel gains, $\mu_{H_R} = N\mu_Z$ and $\sigma_{H_R}^2 = N\sigma_Z^2$.

Fig. 2 shows the PDF derived in (17) with rounded parameter a and evaluates its accuracy by comparing it with the PDF using the exact values of a . The figure shows that rounding the values of a has a negligible effect on the accuracy of the PDF.

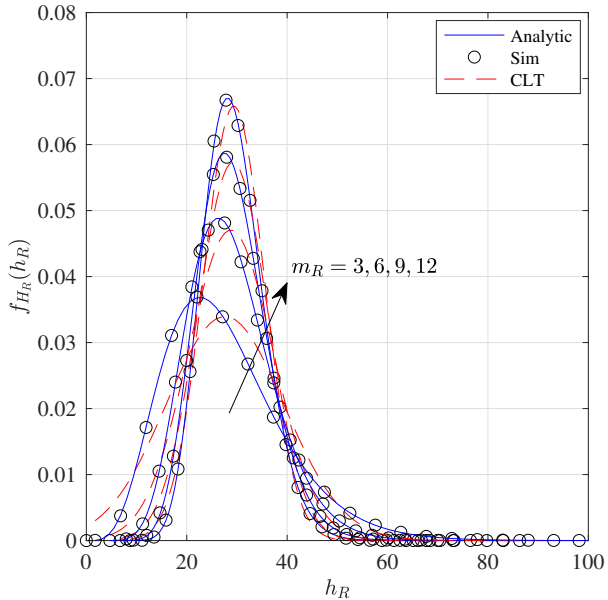


Figure 3: The analytical PDF $f_{H_R}(h_R)$ compared with the CLT and Monte Carlo Simulations for different fading parameter $m_1 = m_2 = m_R$: $N = 30$.

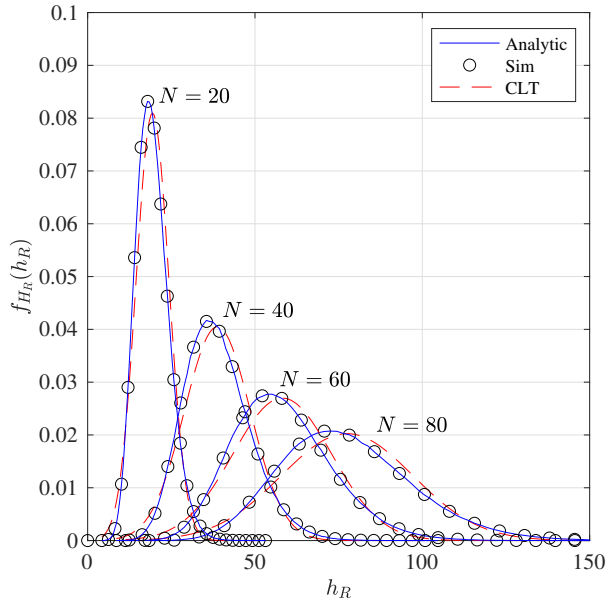


Figure 4: Comparison the analytical PDF $f_{H_R}(h_R)$ with CLT and Monte Carlo Simulation results for different values of N : $m_R = 8$.

Additionally, the difference between the actual values of a and its rounded values can be evaluated numerically by applying the Kullback–Leibler divergence test over 300 samples, which gives a divergence factor of 8.1×10^{-3} for $m_R = 3$, which confirms the accuracy of the approximation. Consequently, in this work, we use the rounded values of a for the sake of simplifying the numerical evaluation.

Proposition 1. Suppose that Z has a gamma distribution with shape and scale parameters of $a \in (0, \infty)$ and $b \in (0, \infty)$, respectively. The distribution of the random variable (RV) Z converges to the normal distribution for high values of N , resulting in

$$\hat{H}_R = \frac{H_R - ab}{\sqrt{ab}}. \quad (18)$$

The PDF of the reflected signal component in (17), the PDF using the CLT, and Monte Carlo simulation results are presented in Figs. 3 and 4. As the figures show, the proposed approximation is more accurate than the approximation based on the CLT regardless of the values of m_R and N . Moreover, the PDF $f_Z(z)$ with fixed and equal fading parameters is shown in Fig. 4 where $N \in \{20, 40, 60, 80\}$. The close matching between the analytical and simulation results corroborates the accuracy of the derived expressions. Furthermore, it can be noted that the fading conditions can be mitigated by increasing N .

The same approach used to derive $F_{H_R}(h_R)$ can be used to derive the PDF and CDF of H_D . Nevertheless, when $F_{H_R}(h_R)$ and $F_{H_D}(h_D)$ are convolved to compute $f_V(v)$, the PDF in (7) makes the analytical approach intractable. Therefore, we propose the following accurate approximation.

Proposition 2. The PDF $f_X(x)$ expressed in (7) can be

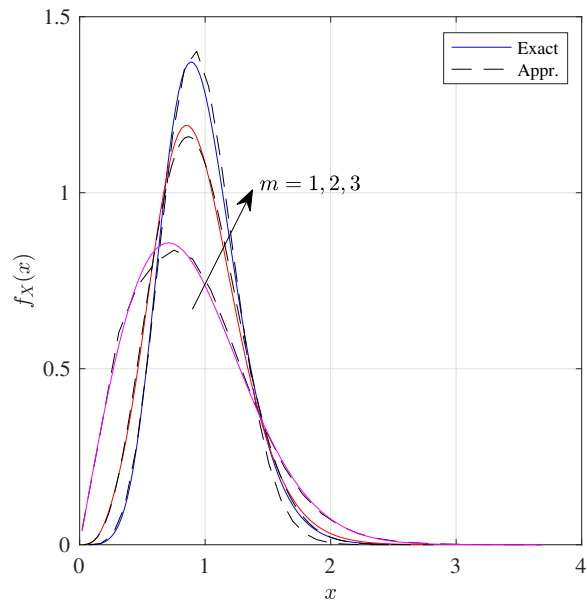


Figure 5: The exact (7), and approximated (19) PDF $f_X(x)$ for $\Omega = 1$ for different values of fading parameter m .

approximated using Laplace method as

$$f_X(x) = \sum_{\nu=1}^5 \frac{\sqrt{\pi}}{\Gamma(m)} \left(\frac{m}{\Omega}\right)^{m-\frac{1}{2}} \frac{\underline{\Delta}_2! a_\nu}{(\nu-1)! \underline{\Delta}^\nu \Gamma(\underline{\Delta}_1)} \times x^{\underline{\Delta}_2} \exp\left(-\frac{x}{\underline{\Delta}}\right) \quad (19)$$

where $\underline{\Delta}_1 = 2m + \nu - 1$, $\underline{\Delta}_2 = \underline{\Delta}_1 - 1$, $a_1 = 0.25482959$, $a_2 = -0.284496736$, $a_3 = 1.421413741$, $a_4 = -1.453152027$, $a_5 = 1.061405429$, $\underline{\Delta} = \frac{p}{2} \sqrt{\frac{\Omega}{m}}$, and $p = 0.3275911$.

Proof. The proof is given in Appendix I. \square

The accuracy of the PDF derived in (19) is assessed in Fig. 5 by comparing it with the exact (7) PDF. For a wide range of x , the figure demonstrates a good agreement between the exact and approximation PDFs. However, at $1.48 \lesssim x \lesssim 2$ and close to the peak of the PDFs, a small divergence is seen in the PDF tail region. Such a deviation is insignificant because it often occurs for a short range of values and is typically minor. On the other hand, the accuracy of the approximation is confirmed by using the Kullback-Leibler divergence test numerically over 300 samples, which yields a divergence factor of 5×10^{-2} for $m_D = 2$.

By using the approximated PDF in (19), the PDF of H_D can be expressed as

$$f_{H_D}(h_D) = \sum_{\nu=1}^5 \mathcal{G}_\nu \frac{1}{\Gamma(\Lambda_1)} h_D^{\Lambda_2} e^{-\frac{h_D}{\Delta}} \quad (20)$$

where $\Lambda_1 = 2m_D + \nu - 1$, $\Lambda_2 = \Lambda_1 - 1$, $\Delta = \frac{p}{2} \sqrt{\frac{\Omega_D}{m_D}}$, and

$$\mathcal{G}_\nu = \frac{\sqrt{\pi}}{\Gamma(m_D)} \left(\frac{m_D}{\Omega_D} \right)^{m_D - \frac{1}{2}} \frac{a_\nu \Lambda_2!}{(\nu - 1)! (\Delta)^\nu}. \quad (21)$$

Because of the superposition of H_D and H_R in (6), the convolution theorem can be applied to (17) and (20) to compute the PDF of V . Therefore,

$$\begin{aligned} f_V(v) &= \int_{-\infty}^{\infty} f_{H_D}(u) f_{H_R}(v-u) du \\ &= \sum_{\nu=1}^5 \frac{\mathcal{G}_\nu}{\Gamma(\Lambda_1) b^a} e^{-\frac{v}{b}} \int_0^v \frac{u^{\Lambda_2}}{(v-u)^{1-a}} e^{\Lambda \Upsilon} du \\ &= \sum_{\nu=1}^5 \frac{\mathcal{G}_\nu v^{\Lambda-1}}{\Gamma(\Lambda) b^a} e^{-\frac{v}{b}} {}_1F_1(\Lambda_1, \Lambda; \Upsilon v) \end{aligned} \quad (22)$$

where $\Lambda = 2m_D + \nu + a - 1$, $\Upsilon = \left(\frac{1}{b} - \frac{1}{\Delta}\right)$.

On the other hand, it can be concluded that (22) can be obtained as a special case from the PDF presented in [63, Eq.28] for a given value of $\kappa - \mu$ shadowed parameters [83, Table. I]. However, deriving various adaptation schemes becomes more complex when utilizing this expression or the PDF presented in [62]. As a result, we derive PDF using Laplace transform approach with the help of partial fraction method, which aids in simplifying mathematical analysis and making it possible to derive closed-form formulas for different adaptation schemes.

D. Moment Generating Function of V

Since H_D and H_R in (6) are independent, the MGF of V is expressed as

$$M_V(s) = M_{H_D}(s) M_{H_R}(s). \quad (23)$$

Applying Laplace transform to (17) and (20), the MGFs of H_R and H_D are respectively given by

$$\begin{aligned} M_{H_R} &= \mathbb{E}_{H_R} [e^{-sh_R}] = \frac{1}{b^a \Gamma(a)} \\ &\times \int_0^\infty h_R^{a-1} \exp\left(-\left(s + \frac{1}{b}\right) h_R\right) dh_R \\ &= \frac{1}{b^a} \left(s + \frac{1}{b}\right)^{-a} \end{aligned} \quad (24)$$

$$\begin{aligned} M_{H_D} &= \mathbb{E}_{H_D} [e^{-sh_D}] = \sum_{\nu=1}^5 \mathcal{G}_\nu \frac{1}{\Gamma(\Lambda_1)} \\ &\times \int_0^\infty h_D^{\Lambda_2} e^{-(s + \frac{1}{\Delta}) h_D} dh_D \\ &= \sum_{\nu=1}^5 \mathcal{G}_\nu \left(s + \frac{1}{\Delta}\right)^{-\Lambda_1}. \end{aligned} \quad (25)$$

By substituting (24), and (25) into (23), the expression for the MGF of V becomes

$$M_V(s) = \sum_{\nu=1}^5 \mathcal{H}_\nu \frac{1}{(1+bs)^a} \frac{1}{(1+\Delta s)^{\Lambda_1}}, \quad \mathcal{H}_\nu = \mathcal{G}_\nu \Delta^{\Lambda_1} \quad (26)$$

E. PDF of the V

The MGF of V in (26) can be rewritten in terms of partial fraction as

$$M_V(s) = \sum_{\nu=1}^5 \mathcal{H}_\nu \left[\sum_{i=1}^a \frac{A_i}{(1+bs)^i} + \sum_{j=1}^{\Lambda_1} \frac{A_j}{(1+\Delta s)^j} \right] \quad (27)$$

where the partial coefficients A_i and A_j are defined in Appendix II.

On the other hand, it can be noted that the MGF and PDF of RV V have the relation

$$f_V(v) = \mathcal{L}^{-1} [M_V(s); v]. \quad (28)$$

By computing the inverse Laplace transform of $M_\nu(s)$ in (27), and using the fact that

$$\mathcal{L}^{-1} \left[\frac{1}{(1+as)^k} \right] = \frac{1}{\Gamma(k)} t^{k-1} e^{-at} \quad (29)$$

the PDF of V can be expressed as

$$f_V(v) = \sum_{\nu=1}^5 \mathcal{H}_\nu [\mathcal{J}_i(v) + \mathcal{J}_j(v)] \quad (30)$$

where $\mathcal{J}_i(v) = \sum_{i=1}^a A_i \frac{v^{i-1} e^{-\frac{v}{b}}}{b^i \Gamma(i)}$ and $\mathcal{J}_j(v) = \sum_{j=1}^{\Lambda_1} A_j \frac{v^{j-1} e^{-\frac{v}{\Delta}}}{\Delta^j \Gamma(j)}$.

F. SNR at the UE Side

The instantaneous SNR at the UE can be expressed as

$$\gamma_Y = \frac{P_s}{N_0} |V|^2 = \bar{\gamma} |V|^2 \quad (31)$$

where \mathcal{P}_s is the transmitted symbol power, N_0 is thermal noise power, and $\bar{\gamma}$ is the average SNR. Therefore, the PDF, CDF and MGF of γ_Y are given by

$$f_{\gamma_Y}(\gamma) = \frac{1}{2\sqrt{\bar{\gamma}}} \sum_{\nu=1}^5 \mathcal{H}_\nu \left[\sum_{i=1}^a A_i \frac{\mathcal{U}_i(\varphi)}{b^i \Gamma(i)} + \sum_{j=1}^{\Lambda_1} A_j \frac{\mathcal{U}_j(\varphi)}{\Delta^j \Gamma(j)} \right] \quad (32)$$

where $\varphi = \sqrt{\frac{\gamma}{\bar{\gamma}}}$, $\mathcal{U}_i(\varphi) = e^{-\frac{\varphi}{b}} \varphi^{i-1}$, and $\mathcal{U}_j(\varphi) = e^{-\frac{\varphi}{\Delta}} \varphi^{j-1}$. For UEs with multiple antennas, i.e., the system is configured as single-input multiple-output (SIMO), then similar to (5), the signal received by the r th antenna can be expressed as,

$$\begin{aligned} Y_{R_r} + Y_{D_r} &= \sqrt{P} e^{-j\theta_{0,r}} \left(\sum_{i=1}^N |h_{i,r}| |g_{i,r}| + |h_{0,r}| \right) s \\ &= (H_{R_r} + H_{D_r}) e^{-j\theta_{0,r}} s = V_r e^{-j\theta_{0,r}} s. \end{aligned} \quad (33)$$

Given that Maximal Ratio Combining (MRC) is adopted, the instantaneous combined SNR can be formulated as $\gamma_C = \sum_{r=1}^{L_R} \gamma_{Y_r}$, where L_R is the number of receiving antennas, and γ_{Y_r} is given in (31). However, deriving the exact PDF of γ_C is intractable, and hence, will be considered in a devoted future work.

G. Amount of fading

The amount of fading (\mathcal{AF}) provides a general metric for the behavior of the fading channel, and it depends on the first and second moments of the SNR,

$$\mathcal{AF} = \frac{\mathbb{E}[\gamma^2]}{\mathbb{E}^2[\gamma]} - 1 \quad (34)$$

where the first and second moments are respectively by

$$\mathbb{E}[\gamma] = \int_0^\infty \gamma f_{\gamma_Y}(\gamma) d\gamma$$

and

$$\mathbb{E}[\gamma^2] = \int_0^\infty \gamma^2 f_{\gamma_Y}(\gamma) d\gamma$$

respectively. By substituting (32) in the first and second moments we obtain

$$\mathbb{E}[\gamma] = \bar{\gamma} \sum_{\nu=1}^5 \mathcal{H}_\nu \left[b^2 \sum_{i=1}^a (i^2 + i) A_i + \Delta^2 \sum_{j=1}^{\Lambda_1} (j^2 + j) A_j \right] \quad (35)$$

and

$$\mathbb{E}[\gamma^2] = \bar{\gamma}^2 \sum_{\nu=1}^5 \mathcal{H}_\nu \left[\sum_{i=1}^a A_i \frac{\Gamma(i+4)}{b^{-4} \Gamma(i)} + \sum_{j=1}^{\Lambda_1} A_j \frac{(j^2 + j)}{\Delta^{-4}} \right]. \quad (36)$$

By substituting (35) and (36) in (34), we obtain a closed-form expression for the amount of fading.

III. CAPACITY ANALYSIS WITH ADAPTIVE TRANSMISSION

Shannon's landmark paper defines channel capacity as the maximum rate at which information can be transmitted over a

channel [84]. In [85]–[87] and the references therein, the Shannon capacity of fading channels under different assumptions about transmitter and receiver channel information has been investigated. These capacity results can be used to assess the efficiency of adaptive and nonadaptive transmission techniques [88], [89] in fading channels in comparison to theoretical maximum performance.

Adaptive transmission is an effective approach that can be used to overcome the influence of fading. Adaptive transmission is based on receiver channel estimation and CSI feedback to the transmitter, where channel state can be mitigated by adjusting the transmit power level, constellation size, symbol/bit rate, coding rate/type or any combination of these parameters [69]. Adapting specific parameters of the transmission signal to the fading channel can contribute to better channel utilization. Some of the common adaptation policies are the OPRA, ORA, CIFR, and TIFR. However, it is worth noting that the adaptive strategy introduces some additional complexity at the transmitter and transmission overhead due to the CSI feedback from the receiver to the transmitter.

This section presents the channel capacity analysis using various adaptive transmission policies, which are the OPRA, ORA, CIFR, and TIFR.

A. Capacity with Adaptive Rate and Fixed Power

The channel capacity in AWGN channels is given by $B \log_2(1 + \mathcal{P}_s/N_0)$. However, when the channel strength varies over time, the transmission rate should be adjusted to avoid exceeding the channel capacity, and hence the optimal rate can be calculated as $B \log_2(1 + \gamma_Y)$. Therefore, the average capacity with optimal rate adaptation to channel fading with constant power is given by [86, Eq. (8)]

$$C_{ORA} = B \int_0^\infty \log_2(1 + \gamma) f_{\gamma_Y}(\gamma) d\gamma. \quad (37)$$

By substituting (32) in (37), transforming $\ln(1 + \gamma)$ into Meijer's [90, 01.04.26.0002.01], and using [91, 07.34 .21 .0088 .01], then C_{ORA} can be evaluated as

$$C_{ORA} = \frac{B}{\ln 2} \sum_{\nu=1}^5 \mathcal{H}_\nu \left[\sum_{i=1}^a \frac{A_i}{\Gamma(i)} U_5 + \sum_{j=1}^{\Lambda_1} \frac{A_j}{\Gamma(j)} U_6 \right] \quad (38)$$

where

$$U_5 = \frac{2^{i-1}}{\sqrt{\pi}} b^i G_{4,2}^{1,4} \left(\frac{1-i}{2}, \frac{2-i}{2}, 1, 1 \mid 4b^2 \bar{\gamma} \right), \quad (39)$$

and

$$U_6 = \frac{2^{j-1}}{\sqrt{\pi}} \Delta^j G_{4,2}^{1,4} \left(1, 1, \frac{1-j}{2}, \frac{2-j}{2} \mid 4\Delta^2 \bar{\gamma} \right). \quad (40)$$

1) *Asymptotic Analysis*: The asymptotic channel capacity with optimal rate adaptation C_{ORA} at low and high SNR will be derived under the assumption that the transmit power is sufficient, and a further simplified expression will be given. Furthermore, at high SNR, the asymptotic performance of C_{ORA} , in terms of multiplexing gain, will be obtained.

Proposition 3. *The asymptotic channel capacity C_{ORA} at high SNR can be expressed as*

$$C_{ORA}^{\infty} \triangleq \mathbb{B} \sum_{\nu=1}^5 \mathcal{H}_{\nu} \left[\sum_{i=1}^a A_i \frac{C_1}{\Gamma(i)} + \sum_{j=1}^{\Lambda_1} A_j \frac{C_2}{\Gamma(j)} \right] \quad (41)$$

where $C_1 = \frac{2}{\ln(2)} b^{-i} \Gamma(i) \left[\Psi(i) + \ln\left(\frac{\sqrt{\gamma}}{b}\right) \right]$ and $C_2 = \frac{2}{\ln(2)} \Delta^{-j} \Gamma(j) \left[\Psi(j) + \ln\left(\frac{\sqrt{\gamma}}{\Delta}\right) \right]$.

Proof. In the high SNR regimes ($\gamma \rightarrow \infty$), the function $\log_2(1 + \gamma) \approx \log_2(\gamma)$. In turn, from (37), we define

$$C_{ORA}^{\infty} \triangleq \mathbb{B} \int_0^{\infty} \log_2(\gamma) f_{\gamma_Y}(\gamma) d\gamma. \quad (42)$$

Substituting (32) in (42) gives

$$C_{ORA}^{\infty} \triangleq \mathbb{B} \sum_{\nu=1}^5 \mathcal{H}_{\nu} \left[\sum_{i=1}^a A_i \frac{C_1}{\Gamma(i)} + \sum_{j=1}^{\Lambda_1} A_j \frac{C_2}{\Gamma(j)} \right] \quad (43)$$

where C_1 and C_2 can be given by

$$C_1 = \frac{1}{2\sqrt{\gamma\bar{\gamma}}} \int_0^{\infty} \log_2(\gamma) \left(\frac{\gamma}{\bar{\gamma}}\right)^{\frac{i-1}{2}} e^{-\frac{1}{b}\sqrt{\frac{\gamma}{\bar{\gamma}}}} d\gamma \quad (44)$$

and

$$C_2 = \frac{1}{2\sqrt{\gamma\bar{\gamma}}} \int_0^{\infty} \log_2(\gamma) \left(\frac{\gamma}{\bar{\gamma}}\right)^{\frac{j-1}{2}} e^{-\frac{1}{\Delta}\sqrt{\frac{\gamma}{\bar{\gamma}}}} d\gamma. \quad (45)$$

Using change of variables, $r = \gamma^2$, and using the integrals identities [66, 8.312-2]

$$\int_0^{\infty} x^{\nu-1} e^{-x} dx = \Gamma(\nu) \quad (46)$$

and [66, 4.352-1]

$$\int_0^{\infty} \ln(x) x^{\nu-1} e^{-x} dx = \Gamma(\nu) \Psi(\nu) \quad (47)$$

(44) and (45) can be expressed as

$$C_1 = \frac{2}{\ln(2)} b^{-i} \Gamma(i) \left[\Psi(i) + \ln\left(\frac{\sqrt{\bar{\gamma}}}{b}\right) \right] \quad (48)$$

and

$$C_2 = \frac{2}{\ln(2)} \Delta^{-j} \Gamma(j) \left[\Psi(j) + \ln\left(\frac{\sqrt{\bar{\gamma}}}{\Delta}\right) \right]. \quad (49)$$

By substituting (48) and (49) into (43), the approximation to the ergodic capacity C_{ORA}^{∞} can be obtained. The asymptotic capacity analysis for other policies can be derived similarly. \square

2) *Multiplexing gain:* The channel capacity expression can be used to derive the multiplexing gain, which can be informally defined as [92],

$$\tilde{G}_m = \frac{C_{ORA}}{\log(\bar{\gamma})}. \quad (50)$$

However, the multiplexing gain is formally defined as [92], [93],

$$G_m = \lim_{\bar{\gamma} \rightarrow \infty} \frac{C_{ORA}}{\log(\bar{\gamma})}. \quad (51)$$

As $\bar{\gamma} \rightarrow \infty$ we obtain $C_{ORA} \approx C_{ORA}^{\infty}$, and therefore G_m can be derived as

$$G_m = \lim_{\bar{\gamma} \rightarrow \infty} \frac{C_{ORA}^{\infty}}{\log(\bar{\gamma})}. \quad (52)$$

Proposition 4. *The multiplexing gain of wireless communication systems with integrated IRS and in the presence of a DL is given by*

$$G_m = \sum_{\nu=1}^5 \mathcal{H}_{\nu} \left[\sum_{i=1}^a A_i b^{-i} + \sum_{j=1}^{\Lambda_1} A_j \Delta^{-j} \right]. \quad (53)$$

Proof. By substituting (43) in (52) and after some mathematical manipulations, the multiplexing channel gain G_m presented in (53) is obtained. \square

As can be noted, it is generally challenging to obtain insights about the behavior of \tilde{G}_m and G_m directly from (53). Therefore, the system performance in terms of multiplexing gain is discussed with the aid of some numerical examples as depicted in Sec. IV.

Proposition 5. *The asymptotic low SNR capacity with Adaptive Rate and Fixed Power expression is given by*

$$C_{ORA}^0 \approx \frac{\mathbb{B}}{\ln 2} \sum_{\nu=1}^5 \mathcal{H}_{\nu} \left[\sum_{i=1}^a \frac{A_i}{\Gamma(i)} \hat{U}_5 + \sum_{j=1}^{\Lambda_1} \frac{A_j}{\Gamma(j)} \hat{U}_6 \right] \quad (54)$$

where $\hat{U}_5 \approx \frac{2^{i+2}}{\sqrt{\pi}} b^{i+2} \Gamma\left(\frac{j+2}{2}\right) \Gamma\left(\frac{j+3}{2}\right) \bar{\gamma}$ and $\hat{U}_6 \approx \frac{2^{j+1}}{\sqrt{\pi}} \Delta^{j+2} \Gamma\left(\frac{j+2}{2}\right) \Gamma\left(\frac{j+3}{2}\right) \bar{\gamma}$.

Proof. At low SNRs, $\bar{\gamma} \rightarrow 0$, the infinite series expansion of the Meijer's G function in (39) and (40) are respectively dominated by the first term as follows [66]

$$G_{4,2}^{1,4} \left(\begin{matrix} 1, 1, \frac{1-i}{2}, \frac{2-i}{2} \\ 1, 0 \end{matrix} \middle| 4b^2 \bar{\gamma} \right) \approx 4b^2 \bar{\gamma} \Gamma\left(\frac{i+2}{2}\right) \times \Gamma\left(\frac{i+3}{2}\right) \quad (55)$$

and

$$G_{4,2}^{1,4} \left(\begin{matrix} 1, 1, \frac{1-j}{2}, \frac{2-j}{2} \\ 1, 0 \end{matrix} \middle| 4\Delta^2 \bar{\gamma} \right) \approx 4\Delta^2 \bar{\gamma} \Gamma\left(\frac{j+2}{2}\right) \times \Gamma\left(\frac{j+3}{2}\right). \quad (56)$$

\square

By substituting (55) and (56) in (39) and (40), and the result in (37), the asymptotic channel capacity is obtained. From Proposition 5, it can be noted that at low SNRs, the C_{ORA} is linearly dependent on $\bar{\gamma}$.

B. Capacity with Power and Rate Adaptation

For the ORA, it is considered that the power is fixed for all transmissions and the rate is the only parameter that can be adapted. However, if the transmit power can be controlled and the average transmit power is constrained by a specific value, then maximizing the capacity implies that the power should not be allocated uniformly for all transmissions. As

shown in [86], optimal power allocation should be performed by pausing the transmission if the SNR drops below a certain threshold. Therefore, given an average transmit power constraint, the channel capacity of a fading channel with received SNR distribution $f_{\gamma_Y}(\gamma)$ and with optimal power and rate adaptation, C_{OPRA} , is given in [86, Eq. (7)] as

$$C_{OPRA} = B \int_{\gamma_0}^{\infty} \log_2 \left(\frac{\gamma}{\gamma_0} \right) f_{\gamma_Y}(\gamma) d\gamma \quad (57)$$

where γ_0 is the optimal cut-off SNR level below which data transmission is paused. Substituting (32) in (57) gives

$$C_{OPRA} = B \sum_{\nu=1}^5 \mathcal{H}_{\nu} [\mathcal{C}_i(\varphi_0) + \mathcal{C}_j(\varphi_0)] \quad (58)$$

where $\mathcal{C}_i(\varphi_0)$, and $\mathcal{C}_j(\varphi_0)$ are given by

$$\mathcal{C}_i(\varphi_0) = \sum_{i=1}^a \frac{A_i}{2b^i \Gamma(i)} \int_{\gamma_0}^{\infty} \log_2 \left(\frac{\gamma}{\gamma_0} \right) \frac{\sqrt{\gamma^i}}{\gamma} \times e^{-\frac{1}{b} \sqrt{\frac{\gamma}{\gamma_0}}} d\gamma \quad (59)$$

and

$$\mathcal{C}_j(\varphi_0) = \frac{1}{2} \sum_{j=1}^{\Lambda_1} \frac{A_j \gamma_0^{-\frac{j}{2}}}{\Delta^j \Gamma(j)} \int_{\gamma_0}^{\infty} \log_2 \left(\frac{\gamma}{\gamma_0} \right) \sqrt{\gamma^{j-2}} \times e^{-\frac{1}{\Delta} \sqrt{\frac{\gamma}{\gamma_0}}} d\gamma. \quad (60)$$

By performing the change of variables $t = \sqrt{\frac{\gamma}{\gamma_0}}$, (59) and (60) become

$$\mathcal{C}_i(\varphi_0) = \sum_{i=1}^a \frac{2A_i}{b^i \Gamma(i)} \varphi_0^i \int_1^{\infty} t^{i-1} \log_2(t) e^{-\frac{\varphi_0}{b} t} dt \quad (61)$$

and

$$\mathcal{C}_j(\varphi_0) = \sum_{j=1}^{\Lambda_1} \frac{2A_j}{\Delta^j \Gamma(j)} \varphi_0^j \int_1^{\infty} t^{j-1} \log_2(t) e^{-\frac{\varphi_0}{\Delta} t} dt. \quad (62)$$

The integral in (61) and (62) can be solved in closed-form as

$$\mathcal{C}_i(\varphi_0) = \frac{2}{\ln(2)} \sum_{i=1}^a \frac{A_i \varphi_0^i}{b^i \Gamma(i)} G_{2,3}^{3,0} \left(\frac{\varphi_0}{b} \left| \begin{matrix} -i+1, -i+1 \\ 0, -i, -i \end{matrix} \right. \right) \quad (63)$$

$$\mathcal{C}_j(\varphi_0) = \sum_{j=1}^{\Lambda_1} \frac{2\varphi_0^j}{\ln(2)} \frac{A_j}{\Delta^j \Gamma(j)} G_{2,3}^{3,0} \left(\frac{\varphi_0}{\Delta} \left| \begin{matrix} -j+1, -j+1 \\ 0, -j, -j \end{matrix} \right. \right) \quad (64)$$

where $G_{p,q}^{m,n}(\cdot)$ denotes Meijer's G function [66, Sec. 9.3], $\varphi_0 = \sqrt{\frac{\gamma_0}{\gamma}}$. By substituting (63) and (64) in (58), the channel capacity C_{OPRA} can be obtained.

On the other hand, the value of γ_0 must satisfy [86, Eq. (6)]

$$\int_{\gamma_0}^{\infty} \left(\frac{1}{\gamma_0} - \frac{1}{\gamma} \right) f_{\gamma_Y}(\gamma) d\gamma = 1. \quad (65)$$

Substituting (32) in (65) and evaluating the integral gives

$$\sum_{\nu=1}^5 \mathcal{H}_{\nu} [\dot{U}_3(\varphi_0) - \dot{U}_4(\varphi_0)] = 1 \quad (66)$$

where $\dot{U}_3(\varphi_0)$ and $\dot{U}_4(\varphi_0)$ are respectively given by

$$\dot{U}_3(\varphi_0) = \frac{1}{\gamma_0} \sum_{i=1}^a \frac{A_i}{\Gamma(i)} \Gamma \left(i, \frac{1}{b} \varphi_0 \right) + \frac{1}{\gamma_0} \sum_{j=1}^{\Lambda_1} \frac{A_j}{\Gamma(j)} \times \Gamma \left(j, \frac{1}{\Delta} \varphi_0 \right) \quad (67)$$

$$\dot{U}_4(\varphi_0) = \frac{1}{\gamma} \sum_{i=1}^a \frac{1}{\Gamma(i) b^2} \Gamma \left(i-2, \frac{1}{b} \varphi_0 \right) + \frac{1}{\gamma} \sum_{j=1}^{\Lambda_1} \frac{1}{\Gamma(j) \Delta^2} \Gamma \left(j-2, \frac{1}{\Delta} \varphi_0 \right). \quad (68)$$

The solution of (66) cannot be evaluated analytically, and hence, it should be solved numerically. Therefore, we define

$$f(\varphi_0) = \sum_{\nu=1}^5 \mathcal{H}_{\nu} [\dot{U}_3(\varphi_0) - \dot{U}_4(\varphi_0)] - 1. \quad (69)$$

It can be noted that $\frac{df}{d\varphi_0}(\varphi_0) \leq 0$ for all $\varphi_0 \geq 0$. Moreover, from (69), it can be observed that $\lim_{\varphi_0 \rightarrow 0^+} f(\varphi_0) = +\infty$ and $\lim_{\varphi_0 \rightarrow +\infty} f(\varphi_0) = -1 \leq 0$. Thus, we conclude that there is a unique γ_0 that satisfies (57).

It is worth noting that applying power adaptation based on instantaneous channel fading requires tracking the fading level at both the transmitter and receiver because the optimal power allocation strategy suggests increasing the transmission power and rate for strong channel conditions while allocating low power and rate for weak channel conditions. Consequently, the system should pause transmission when $\gamma < \gamma_0$, where γ_0 is the optimum transmission SNR threshold. Therefore, the system may experience an outage with probability,

$$P_{out} = \int_0^{\gamma_0} f_{\gamma_Y}(\gamma) d\gamma = 1 - \int_{\gamma_0}^{\infty} f_{\gamma_Y}(\gamma) d\gamma = 1 - F_{\gamma_Y}(\gamma_0). \quad (70)$$

By substituting (32) in (70), the outage probability can be expressed as

$$P_{out} = 1 - \sum_{\nu=1}^5 \mathcal{H}_{\nu} [\mathcal{S}_1(\varphi_0) + \mathcal{S}_2(\varphi_0)] \quad (71)$$

where $\mathcal{S}_1(\varphi_0) = \sum_{i=1}^a \frac{A_i}{\Gamma(i)} \Gamma \left(i, \frac{1}{b} \varphi_0 \right)$ and $\mathcal{S}_2(\varphi_0) = \sum_{j=1}^{\Lambda_1} \frac{A_j}{\Gamma(j)} \Gamma \left(j, \frac{1}{\Delta} \varphi_0 \right)$.

C. Channel Inversion with Fixed Rate

Given that the transmitter and receiver have knowledge of the CSI, then the transmitter can adapt the transmit power to maintain constant fixed received power, or equivalently, fixed SNR, which implies that the transmit power \mathcal{P}_s is selected such

that $\mathcal{P}_s \propto 1/|V|^2$. Thus, this approach is denoted as CIFR, and it is suboptimal because it does not aim at maximizing the channel capacity. This technique uses fixed-rate modulation and a fixed code design because the channel is converted into a time-invariant AWGN channel.

The channel capacity with channel inversion (C_{IFR}) [Bits/Sec] is derived from the AWGN channel case [86, Eq. (9)] as

$$C_{IFR} = B \log_2 \left(1 + \left[\int_0^\infty \frac{1}{\gamma} f_{\gamma_Y}(\gamma) d\gamma \right]^{-1} \right). \quad (72)$$

The integral in (72) can be solved in closed-form by solving

$$\int_0^\infty \frac{1}{\gamma} f_{\gamma_Y}(\gamma) d\gamma = \sum_{\nu=1}^5 \frac{\mathcal{G}_\nu}{\Gamma(\nu)} \left(\frac{1}{b} \right)^{2-\Lambda_1} \frac{\Gamma(\Lambda-2)}{\bar{\gamma}} \times {}_2F_1 \left(\Lambda-2, \Lambda_1, \Lambda, 1 - \frac{b}{\Delta} \right). \quad (73)$$

For channel inversion with a fixed rate, a high transmission power might be needed when the channel introduces a deep fade. Consequently, the channel capacity may deteriorate significantly. Alternatively, we may use a modified inversion policy where the inversion is performed adaptively based on channel fading. Therefore, the inversion is applied only when the channel gain exceeds a certain cut-off value ζ_0 . The capacity with truncated inversion and fixed rate (C_{TIFR}) is reported in [86, Eq. (12)],

$$C_{TIFR} = B \log_2 \left(1 + \left[\int_{\zeta_0}^\infty \frac{1}{\gamma} f_{\gamma_Y}(\gamma) d\gamma \right]^{-1} \right) \times (1 - \dot{P}_{out}) \quad (74)$$

where the cut-off threshold ζ_0 is selected to achieve a specific \dot{P}_{out} as given in (71). Moreover, the integral can be evaluated as

$$\int_{\gamma_0}^\infty \frac{1}{\gamma} f_{\gamma_Y}(\gamma) d\gamma = \frac{1}{\bar{\gamma}} \sum_{\nu=1}^5 \mathcal{H}_\nu \dot{U}_4(\varphi_0) \quad (75)$$

where $\dot{U}_4(\varphi_0)$ is given in (68) except that γ_0 is replaced with ζ_0 .

IV. NUMERICAL RESULTS

This section presents the numerical results generated using the derived analysis for various system and channel parameters. The analytical results are corroborated using Monte Carlo simulation. For each simulation point, 10^6 realizations are generated and averaged. For all the considered scenarios, the channel is assumed to consider a direct and N reflected components, unless it is mentioned otherwise. The case where $N = 0$ corresponds to the scenario where the received signal is composed only of the DL component. The maximum number of elements used is less than 450, which is sufficiently small to allow considering that all communications are performed in the far-field [70]. Because the accuracy of the derived analysis is confirmed in Figs. 6-7, the rest of the numerical results are obtained based on the analytical formulas.

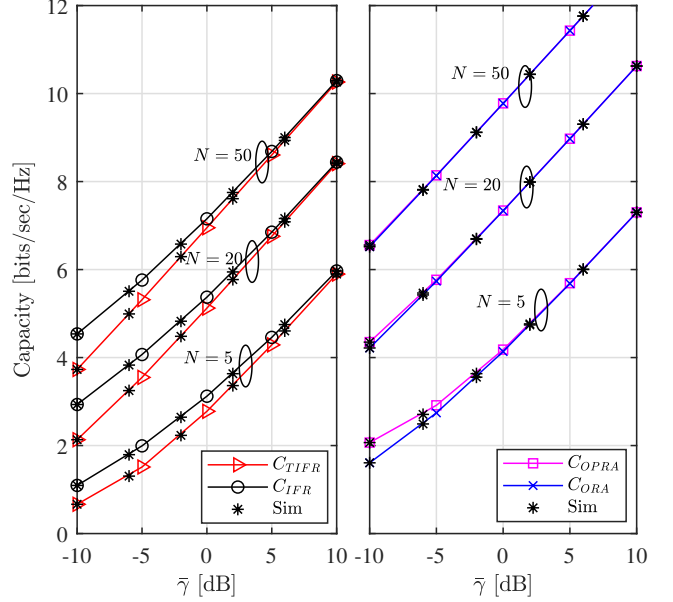


Figure 6: Comparison of adaptation policies versus SNR, where $m_R = 1$, $m_D = 1$.

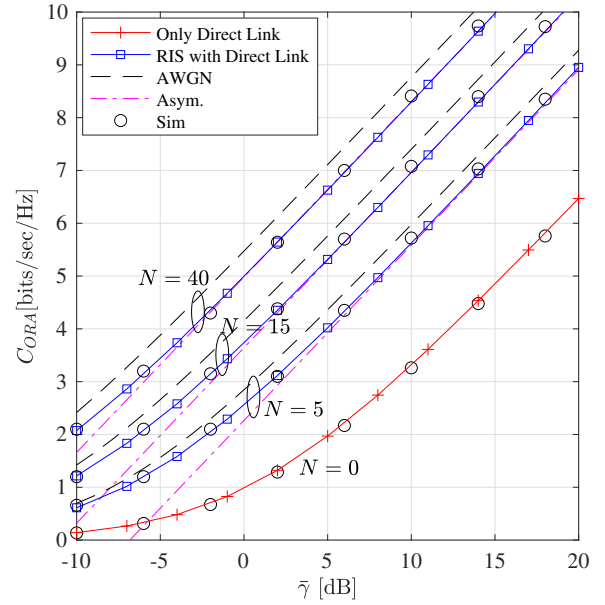


Figure 7: Analytical, asymptotic and simulated C_{ORA} versus SNR for various values of N , $m_R = 4$, and $m_D = 3$.

Fig. 6 compares the capacity for the four transmission strategies versus the average SNR for various N values. It can be noted from the figure that using IRS dilutes the impact of the adaptation process. For example, while the C_{OPRA} offers about 46% improvement over the C_{ORA} at SNR of 0 dB for $N = 5$, but the improvement drops to 15% for $N = 20$. Moreover, C_{OPRA} and C_{ORA} demonstrate near identical performance for a wide range of SNRs. Such performance can be justified by noting that the PDF of the overall received signal envelope experiences mild fading when IRS is used, and thus, adapting the power becomes less critical for the system

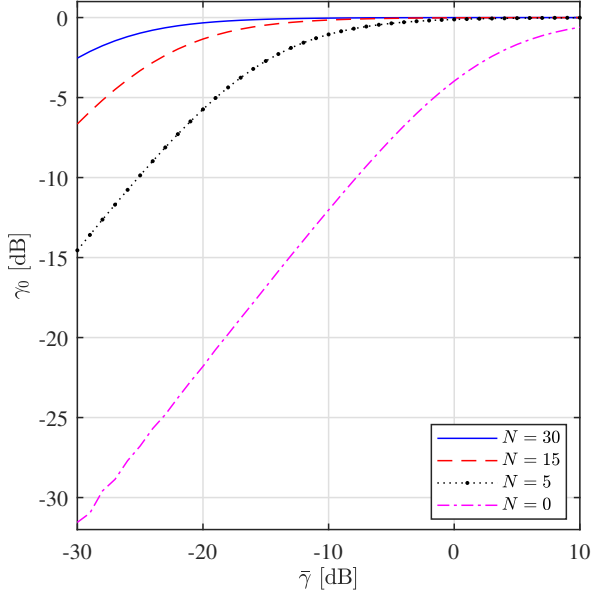


Figure 8: Optimal cut-off SNR γ_0 of the C_{OPRA} versus SNR for various values of N , $m_D = 2$, and $m_R = 2$.

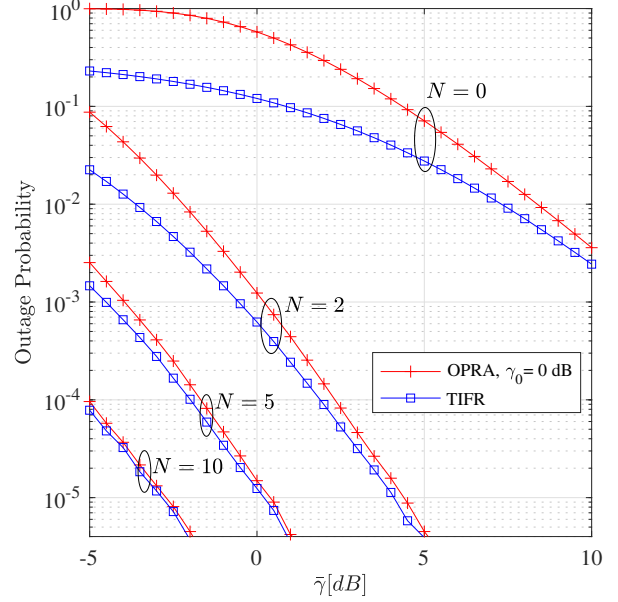


Figure 10: The effect of number of reflecting elements N on Outage probability of the OPRA and TIFR policies with optimum ζ_0 and suboptimal fixed $\gamma_0 = 0$ dB, $m_R = 3$ and $m_D = 3$.

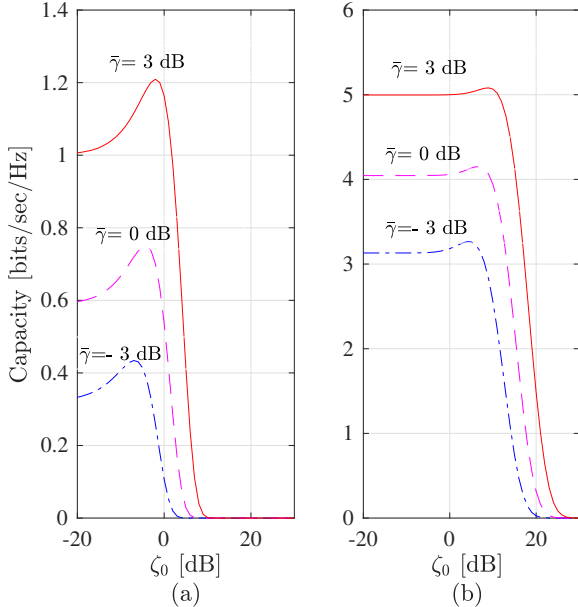


Figure 9: C_{TIFR} versus ζ_0 for $\bar{\gamma} = -3, 0, 3$ dB. (a) $N = 0$ and (b) $N = 5$, $m_R = 2$, $m_D = 2$.

capacity leading to an equivalent performance for the C_{OPRA} and C_{ORA} . The same observation and discussion apply to the C_{TIFR} and C_{IFR} where the coherent combining improves the fading conditions, and thus the truncation process will be rarely applied and the outage probability will be negligible. This behavior is obtained only at high SNRs when $N = 5$ dB, while with IRS it is obtained even at SNR = 10 dB. The figure also shows a close match between the derived analysis and Monte Carlo simulation results. Fig. 7 shows C_{ORA} versus $\bar{\gamma}$ for various values of N . As can be noted from the figure, there is a significant capacity advantage for using IRS-aided

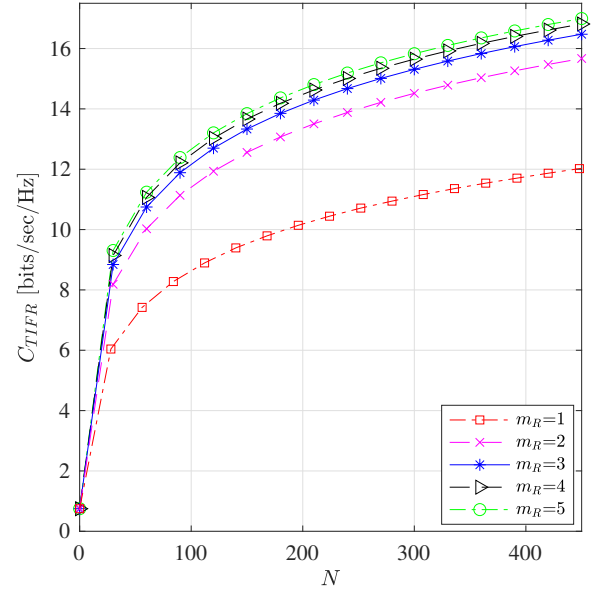


Figure 11: C_{TIFR} versus the number N using various values of m_R , where $\bar{\gamma} = 0$ dB, and $m_D = 2$.

transmission over the DL. As can be noted from the figure, it is generally difficult for the DL alone to provide significant capacity at low SNRs. However, the DL capacity becomes non-negligible at high SNRs. For example, using $N = 5$ at SNR of -10 dB provides about 3.67 fold advantage over the DL case. For $N = 40$, the advantage surges to 13.8 fold. At SNR of 20 dB, the improvement gained using $N = 5$ drops to 0.38 and to 0.8 using $N = 40$. Therefore, the location of the IRS should be optimized to utilize both the direct and reflected links to maximize the channel capacity. More specifically, when the

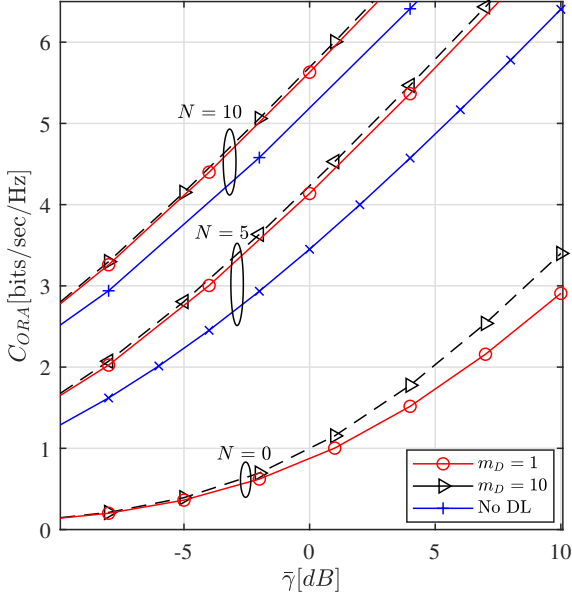


Figure 12: The performance of C_{ORA} with DL and with only IRS [38] for $m_R = 1$ and for various values of N .

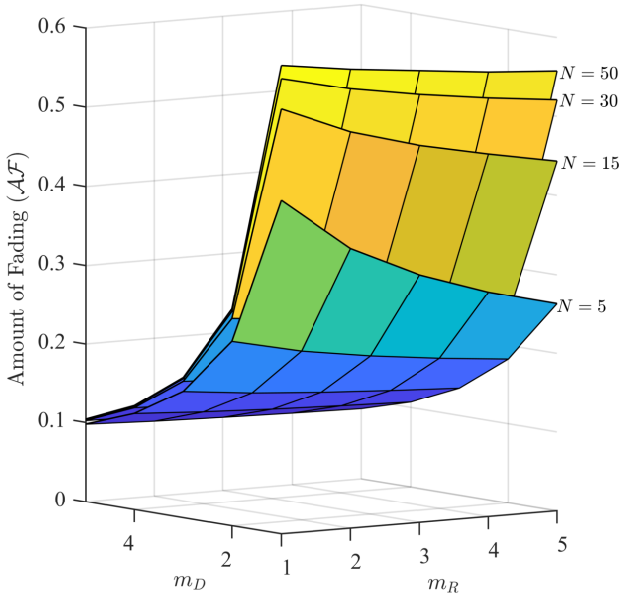


Figure 13: Amount of fading of the $f_{\gamma_Y}(\gamma)$ fading channel versus m_R and m_D , where $\bar{\gamma} = 0$ dB.

number of reflectors is small, the impact of the DL becomes more noticeable. In addition, the channel capacity results are compared with the AWGN Shannon capacity, i.e., $m_{\{\cdot\}} \rightarrow \infty$ for all links. As expected, the figure shows that the AWGN channel capacity is an upper bound for the fading case. On the other hand, the analytical, simulation, and asymptotic C_{ORA} versus SNR for $N \in \{5, 15, 40\}$ are presented. As can be noted from the figure, the analytical and simulation results match very well, which confirms the accuracy of the derived analysis. In addition, the asymptotic analytical results approach the derived approximation at high SNRs.

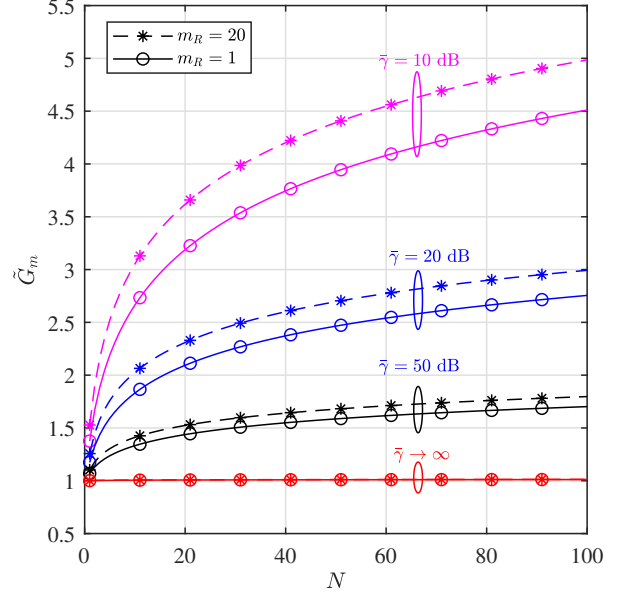


Figure 14: \tilde{G}_m versus N for various values of $\bar{\gamma}$ and m_R for $m_D = 1$.

Fig. 8 depicts the cutoff value γ_0 in (57) versus the average SNR $\bar{\gamma}$, for various values of the N . The γ_0 values are obtained numerically where each value should satisfy the condition in (65) to find the optimal cut-off value that maximizes the average capacity with the OPRA transmission policy. It can be noted from the figure that the optimal γ_0 is proportional to the average SNR $\bar{\gamma}$. At low SNR and small N , the channel quality is poor and hence $\gamma_0 \rightarrow -\infty$ while for high SNR and large N the channel quality is good and hence the cut-off value can be increased such that $\gamma_0 \rightarrow 0$ dB. The impact of increasing N is demonstrated via the convergence of γ_0 to 0 dB for $\bar{\gamma} \gtrsim -20$ dB and $N = 30$. This implies that most of the time the cut-off value is set to 0 dB and no frequent adaptation is needed. Moreover, f_{γ_Y} for $N \gg 1$ is mostly bounded away from the zero region, i.e., $f_{\gamma_Y} \approx 0$, which implies that $\int_{\gamma_0}^{\infty} \log_2\left(\frac{\gamma}{\gamma_0}\right) f_{\gamma_Y}(\gamma) d\gamma \approx \int_0^{\infty} \log_2\left(\frac{\gamma}{\gamma_0}\right) f_{\gamma_Y}(\gamma) d\gamma$ and $\log_2(1 + \gamma) \approx \log_2(\gamma)$. Therefore, using large N values can roughly substitute the power adaption process.

Fig. 9 shows C_{TIFR} versus the SNR threshold ζ_0 using various values of $\bar{\gamma}$. The figure can be used to find the optimal ζ_0 that maximizes C_{TIFR} for each $\bar{\gamma}$. Unlike the C_{OPRA} in Fig. 8, the optimum value ζ_0 can be larger than 0 dB. Comparing Fig. 9 (a) and (b) indicate that for a fixed $\bar{\gamma}$, the optimum ζ_0 increases in the presence of IRS. Moreover, the relatively flat part of the curves in Fig. 9 (b) for ζ_0 less than the optimum value implies that the capacity gain offered by the truncation process is generally small and comes at the expense of a higher outage probability as shown in Fig. 10. Therefore, when IRS is used, channel inversion is considered more efficient than truncated channel inversion because it offers roughly the same capacity with less complexity. It can be seen from the figure that the optimal ζ_0 is proportional to $\bar{\gamma}$.

Fig. 10 shows outage probability (Pout) versus $\bar{\gamma}$ for the

IRS with DL using various values of N . As can be seen from the figure, the optimal and truncated channel inversion offer comparable performance, particularly for $\bar{\gamma} > 0$ dB where the outage probabilities for both schemes converge. The figure also shows that the theoretical and simulation results closely match in the considered range of SNRs. Furthermore, the figure shows that a significant decrease in P_{out} is obtained even when the number of IRS elements is small. The impact of the sensitivity of OPRA to the optimum cut-off is evaluated by using a fixed $\gamma_0 = 0$ dB while using an optimum cut-off SNR ζ_0 for the TIFR. As can be seen from the figure, the TIFR with optimum ζ_0 consistently outperforms the OPRA, particularly for $N \leq 5$. The performance difference between the two schemes vanishes for $N = 10$ because the fixed and optimum γ_0 converge at high SNRs.

Fig. 11 evaluates the effect of varying the number of reflecting elements N on the channel capacity C_{TIFR} for various values of m_R and $m_D = 2$. As can be seen from the figure, the maximum capacity gain is achieved when N increases from 0 to ~ 30 where C_{TIFR} increases, respectively, from 0.74 to 6.01, i.e., improvement 700%. However, when N increases from 30 to 400, the gain is about 100%. As N continues to increase, the capacity gain becomes smaller regardless m_R . Such behavior is obtained because the C_{TIFR} generally follows the log function as depicted in (74). Therefore, the capacity gain is more sensitive to the variation of N when the initial value of N is small. The figure also shows that improving the channel fading from 1 to 2 managed to improve the capacity significantly. However, the improvement starts to saturate for $m_R \geq 4$.

Fig. 12 shows C_{ORA} versus $\bar{\gamma}$ for $N = 0, 5$, and 10. The widely used no DL model [38] is included for comparison purposes. The results are presented for $m_D = 1$ and 10 with and without DL. As can be seen from the figure, the impact of DL can be significant when N is relatively small. For example, for $N = 0$ and $\bar{\gamma} = 0$ dB, the capacity increased by about 1 bit/sec/Hz while it is 0.7 and 0.5 for $N = 5$ and 10, respectively. The impact of m_D is also inversely proportional to N where the impact becomes negligible for $N > 10$.

Fig. 13 shows the \mathcal{AF} versus m_R , m_D , and for various values of N . As can be noted from the figure, the amount of fading decreases whenever m_R or m_D increase, which can be justified by the fact that m_R and m_D are proportional to the channel quality and inversely proportional to \mathcal{AF} . On the contrary, N is proportional to \mathcal{AF} because the second moment of the overall channel is proportional to N . The impact of m_D is more significant than m_R , particularly for large values of N .

Fig. 14 shows the behavior of \tilde{G}_m and G_m versus N . As can be noted from the figure, \tilde{G}_m is monotonically increasing versus N for finite values of $\bar{\gamma}$. Moreover, the improvement is inversely proportional to $\bar{\gamma}$. For $\bar{\gamma} \rightarrow \infty$, that is G_m , the improvement vanishes and $\tilde{G}_m \approx 1 \forall N$. Such results imply that the impact of the IRS deployment is significant only at low SNRs. When SNR is increased significantly, the impact of the IRS becomes less significant because the increase in SNR provides the same effect as the increase in N . The figure also

considers two drastically different values of m_R , which are 1 and 20. As can be noted, the \tilde{G}_m sensitivity to m_R decreases by increasing $\bar{\gamma}$ and it becomes negligible for G_m , i.e., $\bar{\gamma} \rightarrow \infty$. The results were also obtained for various values of m_D , nevertheless, the difference from the case where $m_D = 1$ is negligible, and thus the results are not included in the figure.

V. CONCLUSIONS AND FUTURE WORK

This paper developed and presented a new analytical framework to evaluate the performance of IRS-based communications in the presence of a DL. The MGF, PDF, and CDF of the SNR at the UE were derived and used to derive closed-form expressions for the outage probability, amount of fading, and channel capacity using various adaptive power and rate transmission schemes. The channel between the BS and UE is modeled as a cascaded Nakagami- m fading channel while the DL channel is modeled as Nakagami- m . Due to the intractability of deriving the exact distributions, an accurate approximation is derived and used to derive unified closed-form expressions for the system capacity with channel inversion and fixed rate transmission, optimum power and rate adaptation, and truncated inversion with a fixed rate. The obtained analytical and simulation results demonstrated that the derived approximation provides near-exact results. To gain more insight into the capacity of the system, the asymptotic results are used to quantify the achievable multiplexing gain using the IRS. The derived expressions were used to provide an in-depth understanding of the IRS system capacity in the presence of a DL.

The obtained analytical and simulation results show that the direct link can impact the channel capacity gain obtained by IRS, and hence, should be taken into consideration during the system design. Furthermore, the results demonstrated that adopting the power and rate adaption with IRS is generally different from those in conventional systems. In particular, the impact of the adaptation process may be less significant in the presence of IRS. Monte Carlo simulation was used to validate all the expressions derived. The channel quality between the BS and UE demonstrated a significant impact where the capacity in certain scenarios may drop by about 25%. The gain of increasing the number of reflecting elements showed that the maximum gain is achieved when the number of elements is roughly increased to 100, while for a larger number of reflecting elements the capacity gain becomes small. For example, increasing the number of elements from 200 to 400 improved the gain only by 17%. The results also demonstrated that the gain improvement versus the number of reflecting elements is proportional to the channel quality.

Although there is extensive research on IRS-assisted communications, there are still several research problems that require further investigation. In particular, evaluating the IRS system resilience in the presence of various practical limitations such as the UE mobility, carrier frequency synchronization errors, and imperfect phases estimation and compensation. The high channel capacity that IRS may offer implies that very large modulation orders can be used. However, high-order modulations are highly sensitive to synchronization and

other system and channel errors. Consequently, various optimization problems can be formulated to optimize the system performance in terms of cost, complexity, energy efficiency, and error performance. Evaluating the performance of the considered adaptation processes is an interesting problem when the objective is to maximize the network sum-rate. In such cases, the phase of the IRS elements, power, and rate for each user should be jointly assigned.

VI. APPENDICES

APPENDIX I: PROOF OF PROPOSITION 2

The PDF of Nakagami- m distribution is expressed as

$$f_X(x) = 2 \left(\frac{m}{\Omega}\right)^m \frac{1}{\Gamma(m)} x^{2m-1} e^{-\frac{m}{\Omega}x^2} \quad (76)$$

by using [94, eq.2.2.1.7], the Laplace transform of RV X can be written as

$$\begin{aligned} f_X(s) &= \frac{2}{\Gamma(m)} \left(\frac{m}{\Omega}\right)^m \mathcal{L} \left[x^{2m-1} e^{-\frac{m}{\Omega}x^2} \right] \\ &= \frac{\sqrt{\pi}}{\Gamma(m)} \left(\frac{m}{\Omega}\right)^{m-\frac{1}{2}} (-1)^{2m-1} \\ &\quad \times \frac{d^{2m-1}}{ds^{2m-1}} \left(\operatorname{erfc} \left(\sqrt{\frac{\Omega}{4m}} s \right) e^{\frac{\Omega}{4m}s^2} \right). \end{aligned} \quad (77)$$

The complementary error function and error function have the relation

$$\operatorname{erfc}(x) = 1 - \operatorname{erf}(x) \quad (78)$$

where the error function can be approximated using [68, eq.7.1.26],

$$\begin{aligned} \operatorname{erf} \left(\sqrt{\frac{\Omega}{4m}} s \right) &= 1 - (a_1 t + a_2 t^2 + a_3 t^3 + a_4 t^4 + a_5 t^5) \\ &\quad \times e^{-\frac{\Omega}{4m}s^2} + \epsilon \left(\sqrt{\frac{\Omega}{4m}} s \right) \end{aligned} \quad (79)$$

where $t = \frac{1}{1+\Delta s}$, $|\epsilon(x)| \leq 1.5 \times 10^{-7}$, $a_1 = 0.25482959$, $a_2 = -0.284496736$, $a_3 = 1.421413741$, $a_4 = -1.453152027$, and $a_5 = 1.061405429$. By substituting (79) in (78) and substituting the result in (77), then the Laplace transform of X becomes

$$\begin{aligned} f_X(s) &= \frac{\sqrt{\pi}}{\Gamma(m)} \left(\frac{m}{\Omega}\right)^{m-\frac{1}{2}} (-1)^{2m-1} \\ &\quad \times \frac{d^{2m-1}}{ds^{2m-1}} (a_1 t + a_2 t^2 + a_3 t^3 + a_4 t^4 + a_5 t^5) \\ &= \sum_{\nu=1}^5 \frac{\sqrt{\pi}}{\Gamma(m)} \left(\frac{m}{\Omega}\right)^{m-\frac{1}{2}} (-1)^{2m-1} \\ &\quad \times \frac{d^{2m-1}}{ds^{2m-1}} \left(\frac{a_\nu}{(1+\Delta s)^\nu} \right). \end{aligned} \quad (80)$$

By using

$$\frac{d^{2m-1}}{ds^{2m-1}} \left(\frac{1}{(1+\Delta s)^\nu} \right) = \frac{(-1)^{2m-1} (2m+\nu-2)! \Delta^{2m-1}}{(\nu-1)! (1+\Delta s)^{2m-1+\nu}} \quad (81)$$

and taking inverse Laplace transform

$$\begin{aligned} \mathcal{L}^{-1} \left(\frac{1}{(1+\Delta s)^{2m-1+\nu}} \right) &= \frac{1}{\Delta \Gamma(2m+\nu-1)} \left(\frac{1}{\Delta} \right)^{2m+\nu-2} \\ &\quad \times x^{2m+\nu-2} e^{-\frac{x}{\Delta}}. \end{aligned} \quad (82)$$

Then (7) can be obtained.

APPENDIX II: DERIVE THE MGF USING THE PARTIAL FRACTIONS METHOD

In this appendix, we will apply partial fraction decomposition on (26) to derive a closed-form expression for the MGF that facilitates closed-form expression of the channel capacity. The corresponding MGF of V is given by

$$M_V(s) = \sum_{\nu=1}^5 \mathcal{H}_\nu \frac{1}{(1+bs)^a} \frac{1}{(1+\Delta s)^{\Lambda_1}}. \quad (83)$$

One could image $M_V(s)$ in a form the sum of partial fractions as follows

$$M_V(s) = \sum_{\nu=1}^5 \mathcal{H}_\nu \left[\sum_{i=1}^a \frac{A_i}{(1+bs)^i} + \sum_{j=1}^{\Lambda_1} \frac{A_j}{(1+\Delta s)^j} \right]. \quad (84)$$

Multiplying both sides in (84) by $(1+bs)^a$, taking the derivative of both sides of result up to $a-i$ and using (81), the partial fraction coefficients A_i is given by

$$\begin{aligned} A_i &= \frac{b^{i-a}}{(a-i-1)!} \frac{\partial^{a-i}}{\partial s^{a-i}} \left[M_V(s) (1+bL_{RS})^a \right] \Big|_{t=-\frac{1}{b}} \\ &= \frac{\left(-\frac{\Delta}{b}\right)^{a-i}}{(a-i)!} \frac{(\Lambda-i-1)!}{(\Lambda_2)!} \frac{1}{\left(1-\frac{\Delta}{b}\right)^{\Lambda-i}}. \end{aligned} \quad (85)$$

Similarly, to evaluate the partial fraction coefficient A_j , we multiply both sides in (84) by $(1+\Delta L_{DS})^{\Lambda_1}$, where

$$\begin{aligned} A_j &= \frac{\Delta^{j-\Lambda_1}}{(\Lambda_1-j)!} \frac{\partial^{\Lambda_1-j}}{\partial s^{\Lambda_1-j}} \left[M_V(s) (1+\Delta L_{DS})^{\Lambda_1} \right] \Big|_{t=-\frac{1}{\Delta}} \\ &= \frac{\left(-\frac{b}{\Delta}\right)^{\Lambda_1-j}}{(\Lambda_1-j)!} \frac{(\Lambda-i-1)!}{(a-1)!} \frac{1}{\left(1-\frac{b}{\Delta}\right)^{\Lambda-j}}. \end{aligned} \quad (86)$$

REFERENCES

- [1] "Cisco annual Internet report (2018–2023)," Cisco, Tech. Rep., 2020, an optional note. [Online]. Available: <https://www.cisco.com/c/en/us/solutions/collateral/executive-perspectives/annual-internet-report/white-paper-c11-741490.pdf>.
- [2] X. Tan, Z. Sun, D. Koutsonikolas, and J. M. Jornet, "Enabling indoor mobile millimeter-wave networks based on smart reflect-arrays," in *IEEE INFOCOM 2018 - IEEE Conf. on Computer Communications*, 2018, pp. 270–278.
- [3] N. S. Perović, M. D. Renzo, and M. F. Flanagan, "Channel capacity optimization using reconfigurable intelligent surfaces in indoor mmwave environments," in *IEEE Int. Conf. on Commun. (ICC)*, 2020, pp. 1–7.
- [4] M. A. ElMossallamy *et al.*, "Reconfigurable intelligent surfaces for wireless communications: Principles, challenges, and opportunities," *IEEE Trans. Cogn. Commun. Netw.*, vol. 6, no. 3, pp. 990–1002, 2020.
- [5] E. Basar *et al.*, "Wireless communications through reconfigurable intelligent surfaces," *IEEE Access*, vol. 7, pp. 116753–116773, 2019.
- [6] T. Nguyen *et al.*, "UAV-aided aerial reconfigurable intelligent surface communications with massive MIMO system," *IEEE Trans. Cogn. Commun. Netw.*, vol. 8, no. 4, pp. 1828–1838, 2022.

- [7] C. Liaskos *et al.*, "A new wireless communication paradigm through software-controlled metasurfaces," *IEEE Commun. Mag.*, vol. 56, no. 9, pp. 162–169, 2018.
- [8] T. Nguyen *et al.*, "Intelligent-reflecting-surface-aided bidirectional full-duplex communication system with imperfect self-interference cancellation and hardware impairments," *IEEE Syst. J.*, vol. 17, no. 1, pp. 1352–1362, 2022.
- [9] X. Xie, H. Tang, H. Yang, Q. Huang, and D. Pu, "Intelligent reflecting surface assisted wireless information and power transfer with X-duplex for 6G networks," *IEEE Syst. J.*, vol. 16, no. 4, pp. 5894–5905, 2021.
- [10] Z.-M. Jiang, M. Rihan, P. Zhang, L. Huang, Q. Deng, J. Zhang, and E. M. Mohamed, "Intelligent reflecting surface aided dual-function radar and communication system," *IEEE Syst. J.*, vol. 16, no. 1, pp. 475–486, 2022.
- [11] Q. Wu and R. Zhang, "Towards smart and reconfigurable environment: Intelligent reflecting surface aided wireless network," *IEEE Commun. Mag.*, vol. 58, no. 1, pp. 106–112, 2020.
- [12] A.-A. A. Boulougorgos and A. Alexiou, "Performance analysis of reconfigurable intelligent surface-assisted wireless systems and comparison with relaying," *IEEE Access*, vol. 8, pp. 94463–94483, 2020.
- [13] M. Di Renzo *et al.*, "Smart radio environments empowered by reconfigurable intelligent surfaces: How it works, state of research, and the road ahead," *IEEE J. Select. Areas Commun.*, vol. 38, no. 11, pp. 2450–2525, 2020.
- [14] J. Huang, C.-X. Wang, Y. Sun, R. Feng, J. Huang, B. Guo, Z. Zhong, and T. J. Cui, "Reconfigurable intelligent surfaces: Channel characterization and modeling," *Proc. IEEE*, vol. 110, no. 9, pp. 1290–1311, 2022.
- [15] M. Di Renzo *et al.*, "Reconfigurable intelligent surfaces vs. relaying: Differences, similarities, and performance comparison," *IEEE open J. Commun. Soc.*, vol. 1, pp. 798–807, 2020.
- [16] H. Jiang, M. Mukherjee, J. Zhou, and J. Lloret, "Channel modeling and characteristics for 6G wireless communications," *IEEE Network*, vol. 35, no. 1, pp. 296–303, 2021.
- [17] B. Xiong, Z. Zhang, and H. Jiang, "Reconfigurable intelligent surface for mmwave mobile communications: What if LoS path exists?" *IEEE Wireless Commun. Lett.*, vol. 12, no. 2, pp. 247–251, 2023.
- [18] Y. Gao, J. Xu, W. Xu, D. W. K. Ng, and M.-S. Alouini, "Distributed IRS with statistical passive beamforming for MISO communications," *IEEE Wireless Commun. Lett.*, vol. 10, no. 2, pp. 221–225, 2021.
- [19] S. Zhang and R. Zhang, "Capacity characterization for intelligent reflecting surface aided MIMO communication," *IEEE J. Sel. Areas Commun.*, vol. 38, no. 8, pp. 1823–1838, 2020.
- [20] Q. Wu and R. Zhang, "Beamforming optimization for wireless network aided by intelligent reflecting surface with discrete phase shifts," *IEEE Trans. Commun.*, vol. 68, no. 3, pp. 1838–1851, 2020.
- [21] M. NAKAGAMI, "The m -distribution—A general formula of intensity distribution of rapid fading," in *Statistical Methods in Radio Wave Propagation*, W. HOFFMAN, Ed. Pergamon, 1960, pp. 3–36.
- [22] K.-W. Yip and T.-S. Ng, "A simulation model for Nakagami- m fading channels, $m < 1$," *IEEE Trans. Commun.*, vol. 48, no. 2, pp. 214–221, 2000.
- [23] H. Yang *et al.*, "A programmable metasurface with dynamic polarization, scattering and focusing control," *Scientific Reports*, vol. 6, 2016.
- [24] N. Kaina, M. Dupre, G. Lerosey, and M. Fink, "Shaping complex microwave fields in reverberating media with binary tunable metasurfaces," *Scientific Reports*, vol. 4, 2014.
- [25] C. Huang, A. Zappone, G. C. Alexandropoulos, M. Debbah, and C. Yuen, "Reconfigurable intelligent surfaces for energy efficiency in wireless communication," *IEEE Trans. Wireless Commun.*, vol. 18, no. 8, pp. 4157–4170, 2019.
- [26] L. Du, J. Ma, Q. Liang, C. Li, and Y. Tang, "Capacity characterization for reconfigurable intelligent surfaces assisted wireless communications with interferer," *IEEE Trans. Commun.*, vol. 70, no. 3, pp. 1546–1558, 2022.
- [27] S. Zhang and R. Zhang, "Intelligent reflecting surface aided multi-user communication: Capacity region and deployment strategy," *IEEE Trans. Commun.*, vol. 69, no. 9, pp. 5790–5806, 2021.
- [28] C. Pan, H. Ren, K. Wang, W. Xu, M. ElKashlan, A. Nallanathan, and L. Hanzo, "Multicell MIMO communications relying on intelligent reflecting surfaces," *IEEE Trans. Wireless Commun.*, vol. 19, no. 8, pp. 5218–5233, 2020.
- [29] M. Al-Jarrah, A. Al-Dweik, E. Alsusa, Y. Iraqi, and M.-S. Alouini, "On the performance of IRS-assisted multi-layer UAV communications with imperfect phase compensation," *IEEE Trans. Commun.*, vol. 69, no. 12, pp. 8551–8568, 2021.
- [30] P. Wang, J. Fang, X. Yuan, Z. Chen, and H. Li, "Intelligent reflecting surface-assisted millimeter wave communications: Joint active and passive precoding design," *IEEE Trans. Veh. Technol.*, vol. 69, no. 12, pp. 14960–14973, 2020.
- [31] A. Almohamad *et al.*, "Smart and secure wireless communications via reflecting intelligent surfaces: A short survey," *IEEE open J. Commun. Soc.*, vol. 1, pp. 1442–1456, 2020.
- [32] Q. Wu and R. Zhang, "Intelligent reflecting surface enhanced wireless network via joint active and passive beamforming," *IEEE Trans. Wireless Commun.*, vol. 18, no. 11, pp. 5394–5409, 2019.
- [33] Y.-C. Liang *et al.*, "Large intelligent surface/antennas (LISA): Making reflective radios smart," *J. Commun. Inf. Networks*, vol. 4, no. 2, pp. 40–50, 2019.
- [34] V. C. Thirumavalavan and T. S. Jayaraman, "BER analysis of reconfigurable intelligent surface assisted downlink power domain NOMA system," in *2020 Int. Conf. on Communication Systems Networks (COMSNETS)*, 2020, pp. 519–522.
- [35] M. Aldababsa, A. M. Salhab, A. A. Nasir, M. H. Samuh, and D. B. da Costa, "Multiple RISs-aided networks: Performance analysis and optimization," *IEEE Trans. Veh. Technol.*, vol. 72, no. 6, pp. 7545–7559, 2023.
- [36] M.-A. Badiu and J. P. Coon, "Communication through a large reflecting surface with phase errors," *IEEE Commun. Lett.*, vol. 9, no. 2, pp. 184–188, 2020.
- [37] L. Yang, F. Meng, Q. Wu, D. B. da Costa, and M.-S. Alouini, "Accurate closed-form approximations to channel distributions of RIS-aided wireless systems," *IEEE Commun. Lett.*, vol. 9, no. 11, pp. 1985–1989, 2020.
- [38] A. M. Salhab and M. H. Samuh, "Accurate performance analysis of reconfigurable intelligent surfaces over Rician fading channels," *IEEE Wireless Commun. Lett.*, vol. 10, no. 5, pp. 1051–1055, 2021.
- [39] M. Jung, W. Saad, Y. Jang, G. Kong, and S. Choi, "Performance analysis of large intelligent surfaces (liss): Asymptotic data rate and channel hardening effects," *IEEE Trans. Wireless Commun.*, vol. 19, no. 3, pp. 2052–2065, 2020.
- [40] E. Basar, "Transmission through large intelligent surfaces: A new frontier in wireless communications," *European Conf. on Networks and Communications (EuCNC)*, pp. 112–117, 2019.
- [41] M. Jung, W. Saad, Y. Jang, G. Kong, and S. Choi, "Reliability analysis of large intelligent surfaces (LISs): rate distribution and outage probability," *IEEE Wireless Commun. Lett.*, vol. 8, no. 6, pp. 1662–1666, 2019.
- [42] K. Odeyemi, P. Owolawi, and O. Olakanmi, "Reconfigurable intelligent surface in wireless-powered interference-limited communication networks," *Symmetry*, vol. 13, no. 6, 2021.
- [43] D. Kudathanthirige, D. Gunasinghe, and G. Amarasinghe, "Performance analysis of intelligent reflective surfaces for wireless communication," in *IEEE Int. Conf. Commun. (ICC)*, 2020, pp. 1–6.
- [44] S. Atapattu *et al.*, "Reconfigurable intelligent surface assisted two-way communications: Performance analysis and optimization," *IEEE Trans. Commun.*, vol. 68, no. 10, pp. 6552–6567, 2020.
- [45] I. Trigui, W. Ajib, and W. Zhu, "A comprehensive study of reconfigurable intelligent surfaces in generalized fading," *ArXiv*, vol. abs/2004.02922, 2020.
- [46] I. Trigui *et al.*, "Performance evaluation and diversity analysis of RIS-assisted communications over generalized fading channels in the presence of phase noise," *IEEE Open J. Commun. Soc.*, vol. 3, pp. 593–607, 2022.
- [47] E. Björnson and L. Sanguinetti, "Demystifying the power scaling law of intelligent reflecting surfaces and metasurfaces," in *IEEE 8th Int. Workshop on Computational Advances in Multi-Sensor Adaptive Processing*, 2019, pp. 549–553.
- [48] L. Yang *et al.*, "Indoor mixed dual-hop VLC/RF systems through reconfigurable intelligent surfaces," *IEEE Wireless Commun. Lett.*, vol. 9, no. 11, pp. 1995–1999, 2020.
- [49] L. Yang, F. Meng, J. Zhang, M. O. Hasna, and M. D. Renzo, "On the performance of RIS-assisted dual-hop uav communication systems," *IEEE Trans. Veh. Technol.*, vol. 69, no. 9, pp. 10385–10390, 2020.
- [50] F. Cao, Y. Han, Q. Liu, C.-K. Wen, and S. Jin, "Capacity analysis and scheduling for distributed lis-aided large-scale antenna systems," in *2019 IEEE/CIC Int. Conf. Commun. China (ICCC)*, 2019, pp. 659–664.
- [51] Omer Waqar, "Performance analysis for IRS-aided communication systems with composite fading/shadowing direct link and discrete phase shifts," *Trans. Emerg. Telecommun. Technol.*, vol. 32, no. 10, 2021.

- [52] H. Ibrahim, H. Tabassum, and U. T. Nguyen, "Exact coverage analysis of intelligent reflecting surfaces with Nakagami- m channels," *IEEE Trans. Veh. Technol.*, vol. 70, no. 1, pp. 1072–1076, 2021.
- [53] J. Lyu and R. Zhang, "Spatial throughput characterization for intelligent reflecting surface aided multiuser system," *IEEE Wireless Commun. Lett.*, vol. 9, no. 6, pp. 834–838, 2020.
- [54] I. M. Tanash and T. Riihonen, "Ergodic capacity analysis of RIS-aided systems with spatially correlated channels," in *IEEE Int. Conf. Commun.*, 2022, pp. 3293–3298.
- [55] D. Li, "Ergodic capacity of intelligent reflecting surface-assisted communication systems with phase errors," *IEEE Commun. Lett.*, vol. 24, no. 8, pp. 1646–1650, 2020.
- [56] T. Wang, G. Chen, J. P. Coon, and M.-A. Badiu, "Study of intelligent reflective surface assisted communications with one-bit phase adjustments," in *IEEE Global Commun. Conf. (GLOBECOM)*, 2020, pp. 1–6.
- [57] Q. Tao, J. Wang, and C. Zhong, "Performance analysis of intelligent reflecting surface aided communication systems," *IEEE Commun. Lett.*, vol. 24, no. 11, pp. 2464–2468, 2020.
- [58] B. Tahir, S. Schwarz, and M. Rupp, "Analysis of uplink IRS-assisted NOMA under Nakagami- m fading via moments matching," *IEEE Commun. Lett.*, vol. 10, no. 3, pp. 624–628, 2021.
- [59] L. Yang *et al.*, "Secrecy performance analysis of RIS-aided wireless communication systems," *IEEE Trans. Veh. Technol.*, vol. 69, no. 10, pp. 12 296–12 300, 2020.
- [60] R. C. Ferreira *et al.*, "Bit error probability for large intelligent surfaces under double-Nakagami fading channels," *IEEE Open J. Commun. Soc.*, vol. 1, pp. 750–759, 2020.
- [61] H. Alakoca, M. Babaei, L. Durak-Ata, and E. Basar, "RIS-empowered non-linear energy harvesting communications over Nakagami- m channels," *IEEE Commun. Lett.*, vol. 26, no. 9, pp. 2215–2219, 2022.
- [62] P. Tran *et al.*, "Exploiting multiple RISs and direct link for performance enhancement of wireless systems with hardware impairments," *IEEE Trans. Commun.*, vol. 70, no. 8, pp. 5599–5611, 2022.
- [63] A. Al-Rimawi and A. Al-Dweik, "On the performance of RIS-assisted communications with direct link over κ - μ shadowed fading," *IEEE Open J. Commun. Soc.*, vol. 3, pp. 2314–2328, 2022.
- [64] K. Ying, Z. Gao, S. Lyu, Y. Wu, H. Wang, and M.-S. Alouini, "GMD-based hybrid beamforming for large reconfigurable intelligent surface assisted millimeter-wave massive MIMO," *IEEE Access*, vol. 8, pp. 19 530–19 539, 2020.
- [65] M. Jung, W. Saad, Y. Jang, G. Kong, and S. Choi, "Performance analysis of large intelligent surfaces (LISs): Asymptotic data rate and channel hardening effects," *IEEE Trans. Wireless Commun.*, vol. 19, no. 3, pp. 2052–2065, 2020.
- [66] I. S. Gradshteyn and I. M. Ryzhik, *Table of integrals, series, and products*, 7th ed. Elsevier/Academic Press, Amsterdam, 2007.
- [67] H. Exton, *Multiple hypergeometric functions and applications*. Chichester: Ellis Horwood Ltd., 1976, foreword by L. J. Slater, Mathematics & its Applications.
- [68] M. Abramowitz and I. A. Stegun, *handbook of mathematical functions with formulas, graphs, and mathematical tables*, 9th ed. New York: Dover, 1964.
- [69] M. K. Simon and M. S. Alouini, *Digital Communication over Fading Channels; 2nd ed.* Newark, NJ: Wiley, 2005.
- [70] E. Björnson and L. Sanguinetti, "Power scaling laws and near-field behaviors of massive mimo and intelligent reflecting surfaces," *IEEE Open J. Commun. Soc.*, vol. 1, pp. 1306–1324, 2020.
- [71] T. Shafique, H. Tabassum, and E. Hossain, "Optimization of wireless relaying with flexible UAV-borne reflecting surfaces," *IEEE Trans. Commun.*, vol. 69, no. 1, pp. 309–325, 2021.
- [72] Z. Wang, L. Liu, and S. Cui, "Channel estimation for intelligent reflecting surface assisted multiuser communications: Framework, algorithms, and analysis," *IEEE Trans. Wireless Commun.*, vol. 19, no. 10, pp. 6607–6620, 2020.
- [73] L. Wei *et al.*, "Channel estimation for RIS-empowered multi-user MISO wireless communications," *IEEE Trans. Commun.*, vol. 69, no. 6, pp. 4144–4157, 2021.
- [74] S. Sun and H. Yan, "Small-scale spatial-temporal correlation and degrees of freedom for reconfigurable intelligent surfaces," *IEEE Wireless Commun. Lett.*, vol. 10, no. 12, pp. 2698–2702, 2021.
- [75] S. W. Ellingson, "Path loss in reconfigurable intelligent surface-enabled channels," in *2021 IEEE 32nd Annual Int. Symp. on Personal, Indoor and Mobile Radio Communications (PIMRC)*, 2021, pp. 829–835.
- [76] W. Tang *et al.*, "Wireless communications with reconfigurable intelligent surface: Path loss modeling and experimental measurement," *IEEE Trans. Wireless Commun.*, vol. 20, no. 1, pp. 421–439, 2021.
- [77] E. Björnson, O. Ozdogan, and E. G. Larsson, "Intelligent reflecting surface versus decode-and-forward: How large surfaces are needed to beat relaying?" *IEEE Wireless Commun. Lett.*, vol. 9, no. 2, pp. 244–248, 2020.
- [78] M. A. Al-Jarrah, E. Alsusa, A. Al-Dweik, and M.-S. Alouini, "Performance analysis of wireless mesh backhauling using intelligent reflecting surfaces," *IEEE Trans. Wireless Commun.*, vol. 20, no. 6, pp. 3597–3610, 2021.
- [79] M. Al-Jarrah, E. Alsusa, A. Al-Dweik, and D. K. C. So, "Capacity analysis of IRS-based UAV communications with imperfect phase compensation," *IEEE Wireless Commun. Lett.*, vol. 10, no. 7, pp. 1479–1483, 2021.
- [80] A. A. Abu Dayya and N. C. Beaulieu, "Microdiversity on rician fading channels," *IEEE Trans. Commun.*, vol. 42, no. 6, pp. 2258–2267, 1994.
- [81] N. Kumar and V. Bhatia, "Exact ASER analysis of rectangular QAM in two-way relaying networks over Nakagami- m fading channels," *IEEE Wireless Commun. Lett.*, vol. 5, no. 5, pp. 548–551, 2016.
- [82] F. J. Lopez-Martinez, L. Moreno-Pozas, U. Fernandez-Plazaola, J. F. Paris, E. Martos-Naya, and J. M. Romero-Jerez, "A tractable line-of-sight product channel model: Application to wireless powered communications," in *2018 15th Int. Symp. on Wireless Communication Systems (ISWCS)*, 2018, pp. 1–5.
- [83] L. Moreno-Pozas, F. J. Lopez-Martinez, J. F. Paris, and E. Martos-Naya, "The κ - μ shadowed fading model: Unifying the κ - μ and η - μ distributions," *IEEE Trans. Veh. Technol.*, vol. 65, no. 12, pp. 9630–9641, 2016.
- [84] C. E. Shannon, "A mathematical theory of communication," *The Bell System Technical Journal*, vol. 27, pp. 379–423, 1948.
- [85] W. Lee, "Estimagentte of channel capacity in rayleigh fading environment," *IEEE Trans. Veh. Technol.*, vol. 39, no. 3, pp. 187–189, 1990.
- [86] A. Goldsmith and P. Varaiya, "Capacity of fading channels with channel side information," *IEEE Trans. Inf. Theory*, vol. 43, no. 6, pp. 1986–1992, 1997.
- [87] G. Caire and S. Shamaganti, "On the capacity of some channels with channel state informagnttion," *IEEE Trans. Inf. Theory*, vol. 45, no. 6, pp. 2007–2019, 1999.
- [88] S.-G. Chua and A. Goldsmith, "Variable-rate variable-power MQAM for fading channels," in *Proc. Vehicular Technology Conf. (VTC)*, vol. 2, 1996, pp. 815–819.
- [89] A. Goldsmith and S.-G. Chua, "Adaptive coded modulation for fading channels," *IEEE Trans. Commun.*, vol. 46, no. 5, pp. 595–602, 1998.
- [90] W. R. Inc., "Mathematica, Version 13.0.0," champaign, IL, 2021. [Online]. Available: <http://functions.wolfram.com/01.04.26.0002.01>
- [91] —, "Mathematica, Version 13.0.0," champaign, IL, 2021. [Online]. Available: <http://functions.wolfram.com/07.34.21.0088.01>
- [92] L. Zheng and D. Tse, "Diversity and multiplexing: a fundamental tradeoff in multiple-antenna channels," *IEEE Trans. Inf. Theory*, vol. 49, no. 5, pp. 1073–1096, 2003.
- [93] Y. Zhao, H. Chen, L. Xie, and K. Wang, "Exact and asymptotic ergodic capacity analysis of the hybrid satellite-terrestrial cooperative system over generalised fading channels," *IET Communications*, vol. 12, pp. 1342–1350(8), July 2018.
- [94] A. Prudnikov, Y. Brychkov, and O. Marichev, *Integrals and Series. Vol. 2. Special Functions*, 01 1992, vol. 2.



Ashraf Al-Rimawi (Member, IEEE) received the B.S. degree in electrical engineering from Birzeit University in 2008, the master's degree in wireless communication from the Jordan University of Science and Technology in 2012, and the Ph.D. degree in wireless communication from Bologna University in 2017. During his Ph.D. period, he participated in the H2020 Xecycle Project, Italy. He was a Teaching and Research Assistant with Al-Quds University, Duisburg- Essen University, Jordan University of Science and Technology, and Bologna University. He

is a member of Palestine Communication and Informatics Society (PCIS), and he has been a Lecturer with the Department of Electrical and Computer Engineering, Birzeit University, Palestine, since 2012, where he is currently an Assistant Professor. His research is on the theory and development of wireless communication systems, mathematical modeling and analysis of emerging wireless communication architectures, leading to innovative and/or theoretically optimal new communication techniques. He has published several journal and conference papers in the IEEE Transaction Wireless Communication and strong congress conferences such as VTC and ICC. He is chosen as one of the Reviewers in the IEEE transaction Wireless communication, IEEE Wireless communication letter, and several conferences.



Arafat Al-Dweik received the M.S. (Summa Cum Laude) and Ph.D. (Magna Cum Laude) degrees in electrical engineering from Cleveland State University, Cleveland, OH, USA, in 1998 and 2001, respectively.

He is currently with the Department of Electrical Engineering and Computer Science, Khalifa University, Abu Dhabi, UAE. He also worked at Efficient Channel Coding, Inc., Cleveland, OH, USA, Department of Information Technology, Arab American University, Jenin, Palestine, and the University of

Guelph, ON, Canada. He is a Visiting Research Fellow with the School of Electrical, Electronic, and Computer Engineering, Newcastle University, Newcastle upon Tyne, U.K, and a Research Professor with Western University, London, ON, Canada, and the University of Guelph, Guelph, Canada. He has extensive research experience in various areas of wireless communications that include modulation techniques, channel modeling and characterization, synchronization and channel estimation techniques, OFDM technology, error detection and correction techniques, MIMO, and resource allocation for wireless networks.

Dr Al-Dweik serves as an Associate Editor for the IEEE Transactions on Vehicular Technology and the IET Communications. He is a member of Tau Beta Pi and Eta Kappa Nu. He was awarded the Fulbright scholarship from 1997 to 1999. He was the recipient of the Hijjawi Award for Applied Sciences in 2003, the Fulbright Alumni Development Grant in 2003 and 2005, Dubai Award for Sustainable Transportation in 2016, UAE Leader-Founder Award in 2019. He is a Registered Professional Engineer in the Province of Ontario, Canada.



ALI A. SIDDIG ALI A. SIDDIG received the B.S. and M.S. degrees in electronics engineering (communications) from Sudan University of Science and Technology, Sudan, in 2006 and 2012, respectively, and the Ph.D. degree in wireless and mobile systems from Universiti Sains Malaysia (USM), Pinang, Malaysia, in 2018. He worked as a postdoctoral fellow at American university of Sharjah from Feb-2019 to Feb-2021. He is currently working as a postdoctoral fellow at Khalifa university, Abu Dhabi, UAE. His research interests include cooperative

communications, vehicular communications, and signal processing for wireless communication networks.